Effect of mechanical strain on the transport properties of thin-film composite membranes used in osmotic processes

Jaime A. Idarraga-Mora[a], Alton D. O'Neal[a], Morgan E. Pfeiler[a], David A. Ladner[b], Scott M. Husson[a,*]

[a] Department of Chemical and Biomolecular Engineering, Clemson University, 127 Earle Hall, Clemson, SC 29634, USA

[b] Department of Environmental Engineering and Earth Sciences, Clemson University, 342 Computer Court, Anderson, SC 29625, USA

*Corresponding author: Tel: +1 (864)-656-4502, Fax: +1 (864)-656-0784. Email address: shusson@clemson.edu

Graphical Abstract

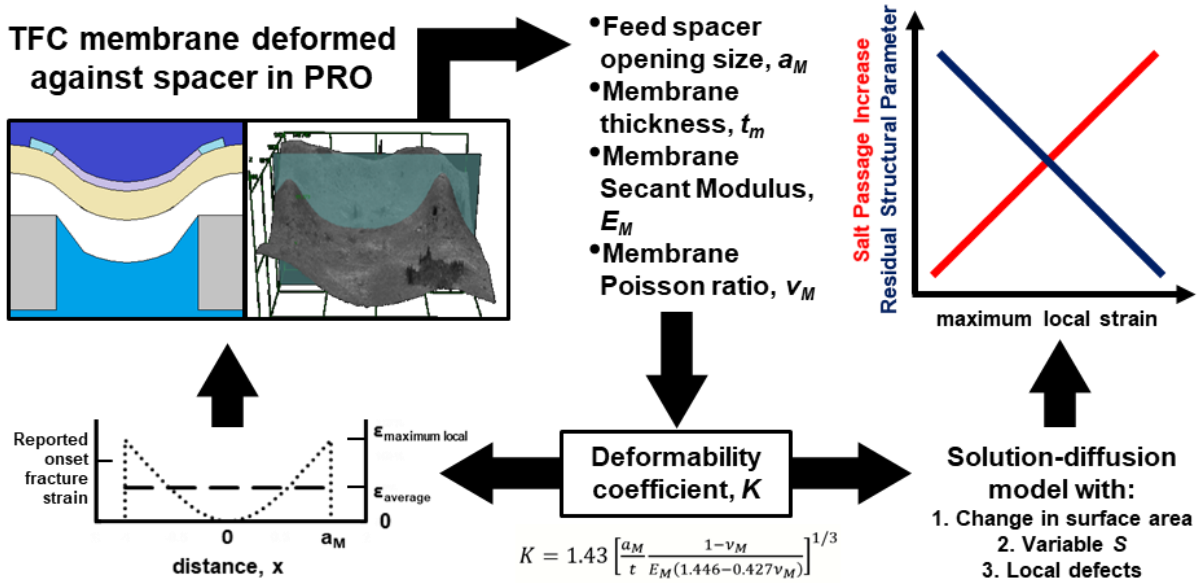

Abstract

In this work, we studied the mechanical behavior of commercial thin-film composite membranes and measured water and salt transport through membranes that were subjected to known degrees of strain. Our aim was to correlate linear strain with transport properties. Firstly, we showed that the global transport properties of the membranes did not change significantly after being subjected to linear strain values that are typical of pressure-retarded osmosis (PRO) operations. Secondly, using a newly developed osmotically-driven burst pressure test for flat sheet membranes, we theorized that the increased salt passage through the membranes was attributable to local deformation and defect formation in the membrane region along the border of the feed spacer opening. Using laser microscopy, we were able to pinpoint the area on the membrane with increased deformation, and to measure the deformation profile. We defined a deformability coefficient to estimate the membrane strain at a known pressure in terms of easily attainable characteristics like opening size, membrane thickness and secant modulus and used it to postulate a solution diffusion model that accounts for defects by considering the deformability of the membrane in the experimental setup. By incorporating membrane deformation into the boundary layer equations used to describe water and salt flux in osmotic processes (OP), the model can describe the observed dependence of salt flux with applied pressure. The model was used to fit our PRO experimental data and numerous data reported in the literature, which revealed that salt passage increases as membrane deformation increases. Along with this effect, there is a lowered mass-transfer resistance, which constitutes the trade-off between mechanical deformation and mass-transfer resistance observed in pressurized OP. Our findings show that the deformability coefficient and our solution diffusion model with defects can serve as guidelines for the design of membranes and modules for pressurized OP such as PRO.

Keywords: solution-diffusion model; membrane deformation; pressure-retarded osmosis; membrane mechanical properties

1. Introduction

Osmotic processes (OP) rely on a difference in osmotic pressure across a membrane to drive fluid flow. Examples of these processes are osmotically-assisted reverse osmosis (OARO) [1], pressure-retarded osmosis (PRO) [2,3], forward osmosis (FO) [4], and pressure-assisted forward osmosis (PAFO) [5,6]. Unlike reverse osmosis (RO), OP suffer from the detrimental effects of internal concentration polarization (ICP). In RO desalination, both water and salt are transported from the high concentration feed to the permeate side of the membrane; however, separation occurs because water moves considerably faster than salt through the membrane. In OP, water and salt move in opposite directions; therefore, the difference in solute concentration (i.e., osmotic pressure) between the two surfaces of the membrane active layer is reduced due to this counterdiffusion of water and salt. ICP derives from a diffusion-limited transport of the solutes through the membrane supporting structures, which include porous support and backing layers in the case of a thin-film composite (TFC) membrane.

Membrane supports often are characterized by means of the structural parameter (S) [7]. This parameter is defined as the effective distance that the solute travels by diffusion across the membrane support. Eq. 1 gives the definition of intrinsic structural parameter in terms of the membrane thickness (t_m), tortuosity (τ) and porosity (φ). According to this equation, reducing thickness and increasing porosity would decrease the effective distance for solute diffusion, which would reduce the detrimental effect of ICP, and thereby yield higher productivity [8]. However, reducing membrane support thickness increases the mechanical tensile load at a given transmembrane pressure. Additionally, increasing porosity reduces both the strength and stiffness

of a membrane support, reducing the load that the membrane can withstand without failure. These considerations suggest that a tradeoff exists between mechanical stability of the membrane support and its productivity, particularly for OP that experience a transmembrane pressure, such as in PRO.

$$S = \frac{t_m \tau}{\varphi} \quad (1)$$

Multiple studies have reported improved PRO performance by controlling the membrane support characteristics that compose the structural parameter while attempting to improve the membrane mechanical properties [9–11]. Other studies have focused on improving the feed spacer and membrane cell design to minimize membrane mechanical deformation during PRO operation [12–14]. These studies have observed that the salt flux during PRO operation increases as transmembrane pressure increases. This increase has been attributed to membrane deformation, both compaction and bending, against the membrane feed spacer. This dependence of salt flux on transmembrane pressure is not predicted by conventional solution-diffusion models used to describe OP [15–17]. Additionally, these models and previous experiments show that an increased apparent salt permeability coefficient (i.e. larger effective salt passage) reduces the water flux across the membrane. Ultimately, this can reduce the power density attainable from the membrane during PRO by up to 50% [14].

Different test methods, models and parameter estimation algorithms have been proposed based on the conventional solution-diffusion models to improve predictability and interpretation of the experimental results in OP [6,14,18–22]. These approaches have tried to address the fact that the membrane transport properties (i.e., water permeance, *A*, salt flux coefficient, *B*, and *S*) change due to membrane deformation by making them mathematically dependent on pressure, or

introducing new parameters that depend on pressure. General observations of these studies are four-fold: (1) *A* and *B* values measured via RO with the membrane on a permeate carrier (as feed spacer) are lower than the case of the membrane on a diamond-shaped feed spacer. (2) *B* increases relatively faster than *A* as transmembrane pressure increases due to loss of selectivity. (3) The structural parameter can either increase or decrease depending on the type of feed spacer used. (4) The membrane will deform to some extent, taking the shape of the spacer regardless of the type of feed spacer used.

Since all previous observations suggest a loss of selectivity due to membrane deformation, efforts have been made to increase membrane mechanical stability. Khraisheh and coworkers [23] reviewed the typical mechanical properties reported for membranes used for water desalination. For polymeric membranes these include the tensile stress-strain curve, the Young's Modulus, yield strength, tensile strength (at break), elongation at break, toughness, and burst strength [23]. However, no clear heuristics have been established to guide improvements in the mechanical properties that are most relevant to minimizing the detrimental effects of membrane deformation on selectivity.

The goals of this work were to study water and salt transport through TFC membranes that were subjected to known degrees of strain and to use the findings to improve the boundary layer equations that describe water and salt flux in osmotic processes. We define failure of the membrane as the loss of selectivity, rather than defining it as irreversible mechanical deformation (i.e., stress on the membrane above its yield or tensile strength), by proposing an osmotically-driven burst pressure test for flat sheet membranes. We demonstrate the importance of knowing the stress-strain curve of the membrane, and highlight that stiffer membrane structures are desirable to avoid reaching a strain above the reported onset fracture strain of the

selective layer [24]. Since membrane deformation has been reported regardless of the feed spacer used, we assumed that the stress on the membranes is above the yield strength of the membrane supporting structure. The implication is that the membrane deformation is not represented by the Young's Modulus (elastic deformation), but instead a secant modulus that can be calculated from the stress-strain diagrams. We propose a transport model to represent the salt and water flux through the membrane more accurately during PRO operation. This model is based on our observations of membrane mechanical deformation and includes the change in surface area; the change in structural parameter; and the creation of non-selective, localized defects. Our model suggests that the changes in surface area and the structural parameter are relatively small. We theorize that generation of local defects has the largest influence on the increased salt passage during PRO operation. Finally, we introduce a deformability coefficient and our solution diffusion model with defects to guide the design of membranes and modules for pressurized OP such as PRO, OARO, and PARO. Inclusion of this deformability coefficient may benefit other niche applications such as patterning RO membranes or high-pressure RO for achieving zero liquid discharge.

2. Experimental

2.1 Materials and chemicals

SEAMAXX and SW30XLE seawater desalination membranes were provided by DuPont Water & Process Solutions (Edina, MN, USA). Before any testing, membrane samples were rinsed with DI water (resistivity > 18.2 MΩ cm) obtained from a Milli-Q water purification system (EMD-Millipore, Burlington, MA) to remove protective coatings. Sodium chloride (NaCl, anhydrous, >99%) was purchased from Sigma Aldrich Inc. (St. Louis, MO, USA). Ethanol (anhydrous) was purchased from Fisher Scientific (Pittsburgh, PA, USA).

2.2 Characterization of TFC membranes

Tensile strength and Young's Modulus of the SEAMAXX and SW30XLE membranes were measured based on the ASTM D882-12 standard [25] using an Instron 1125 Universal Testing Machine (Instron, Norwood, MA, USA). Five measurements were made per sample. Additionally, this machine was used to prepare membrane samples that were preconditioned by applying a defined strain. To do so, a sample was clamped between hydraulic jaws that exerted a pressure of about 100 bar and then extended to apply a target strain value (hold strain). The pressure of 100 bar on the hydraulic jaws was used to avoid jaw slippage that could result in a lower modulus measurement. After reaching the hold strain, the stress was maintained constant for 5 min by an internal controller, and then the sample was released from the hydraulic jaws. For these experiments, a 100 kg load cell was used, the gap between clamping devices (jaws) was kept at 76 mm, the width of the samples was 76 mm, and the pulling rate was 7.6 mm/min. These conditions were modified from the ASTM D882-12 standard to obtain membrane coupons that were testable in our permeation apparatuses. SEAMAXX TFC membranes with the non-woven backings removed (hereafter called backing-free samples) also were subjected to testing. Our aim for using backing-free samples was to differentiate the contributions from each layer in the mechanical behavior of the composite structure. Understanding how each layer contributes can provide insights to improve membrane design that cannot be elucidated by studying the as-received membrane alone. In this case, the gap between jaws was kept at 30 mm, the width of the samples was 10 mm, and the pulling rate was 3 mm/min. At least three measurements were made per sample.

Scanning electron microscopy (SEM) was used to image the top surface of membranes before and after permeation testing to observe changes in the morphology and characterize the

deformed active layers. Samples were sputter coated with gold-palladium for 2 min using an Anatech Hummer® 6.5 (Anatech Limited, Denver, NC, USA). A Hitachi S4800 High Resolution SEM (Hitachi Limited, Tokyo, Japan) was used with an accelerating voltage of 10 kV.

An Olympus LEXT 3D laser confocal microscope OLS4000 (LEXT software version 2.2.3, Olympus Scientific Solutions Americas, Inc., Waltham, MA, USA) was used to visualize and quantify the deformation of membranes tested in PRO mode. This instrument uses a 405 nm laser source with a planar measurement accuracy of ± 2%. We used a 10x objective lens (MPLFLN10X) with a numerical aperture of 0.30. Accuracy in the height measurement was estimated to be ± 5.2 μm of (= 0.2 + L/100 μm, where L is the length of the scan in the z-axis, estimated to be 500 μm). Adjacent images on a sample were taken and stitched together to visualize an area of 11.7 mm × 7.1 mm (83 mm^2). To remove noise, we applied a "jagged surface" correction to every raw image. The maximum deflection was measured by selecting a unit of membrane area on top of a feed spacer opening, which was determined by visualizing the feed spacer wire profile on the membrane surface (see Figure S1 in Supporting Information). Then, this membrane area was surveyed to find the maximum deflection (see Figure 1). Five measurements were made on three different SEAMAXX samples recovered after PRO testing.

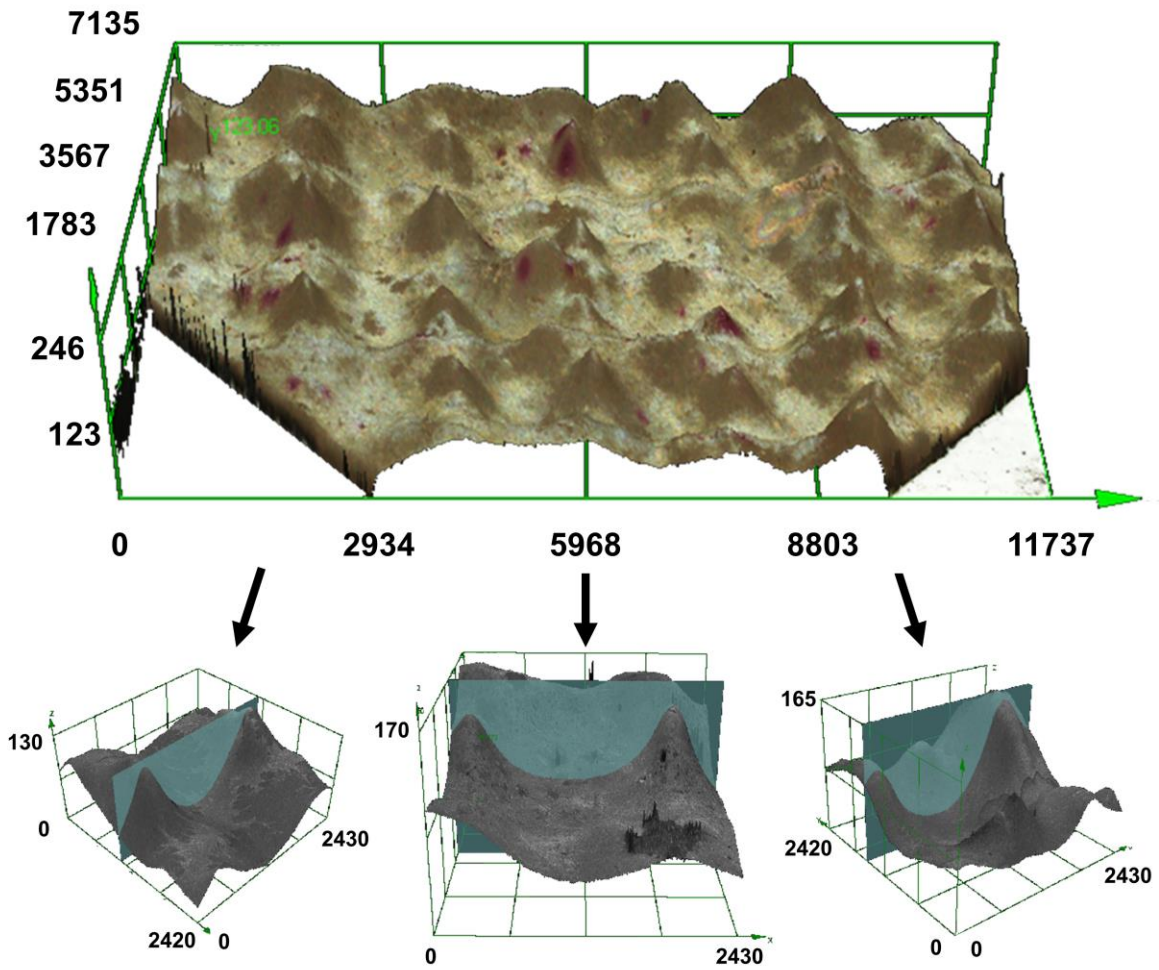

Figure 1. (Top) 3D rendering of a tested membrane coupon used to measure the deflection. Brightness and contrast have been increased by 40% to facilitate observation of features. (Bottom) Examples of membrane section on top of one opening. The blue planes are perpendicular to the wire direction and show the largest deflection. All axis units are in μm.

The thicknesses of the as-received and backing-free TFC membranes were measured with a Mitutoyo 293-340-30 Digital Micrometer (Mitutoyo Corporation, Kawasaki, Japan). Four measurements were taken at different spots per sample.

Burst pressures were measured using a lab-built diffusion cell (see Figure S2 in Supporting Information). Four experiments were conducted for each membrane type. Measurements were

made for as-received SEAMAXX TFC membrane and a backing-free SEAMAXX membrane coupon. The diffusion cell was made of welded PVC piping. The apparatus parts and their specifications are shown in Figure S2. A pressure transmitter (Wika A-10 0-300 psi 4-20 mA, Wika USA, Lawrenceville, GA, USA) was connected to the reducing tee and used to record the pressure inside the cell continuously. During a typical experiment, a water rinsed membrane coupon was installed between the gasket and the bottom flange, with the active layer facing the gasket (commonly called the AL-DS configuration for PRO operation). Plastic bolts and nuts (to avoid corrosion) were used to tighten the two flanges and provide a seal. Approximately 110 mL of 1.5 M NaCl solution were added to the cell while ensuring the removal of any entrapped air, and then the ball valve was closed. The entire cell was placed into a container with 1 L of tap water (resistivity = 2.0 kΩ cm), a stir bar was added, and the container was placed atop a stir plate with a set stirring speed of at least 150 RPM. Finally, a Sensorex CS150TC conductivity probe connected to a Sensorex CX10 transmitter (Sensorex Inc., Garden Grove, CA, USA) was placed into the container and it was used to record the conductivity of the tap water during the experiment. The pressure inside the cell and the conductivity of the tap water were recorded using a NI USB-6001 and a graphic user interface created in NI LabView 2018 (National Instruments, Austin, TX, USA).

2.3 TFC membrane transport property measurements

Water permeance (A) and salt rejection (R) were measured for SEAMAXX and SW30XLE samples that were preconditioned by applying a defined linear strain, as described in Section 2.2. Membrane coupons were cut from a strained sample and soaked in DI water for 5 min to remove protective coatings. The SW30XLE membrane coupons were submerged for 5 min into a 50:50 (v/v) ethanol/water solution before testing to increase its water permeance, and thus reducing the

testing time. This membrane was selected since our previous study showed larger changes in transport properties for SW30XLE than SEAMAXX membranes upon alcohol wetting [26]. The testing was done with a direct-flow apparatus that connects to three Sterlitech HP4750 stirred cells (membrane active area = 14.6 cm^2, Sterlitech Corporation, Kent, WA, USA) in parallel. The cells were filled with a 2000 ppm NaCl feed solution (osmotic pressure of 1.7 bar at 25°C) and set on stir plates with stirring speeds no lower than 120 RPM. The system was pressurized up to 17.2 bar using compressed air. The system was operated for 30 min after permeation began to achieve a constant flowrate. Thereafter, the mass of permeate (m_P) was recorded for a time (t). The water flux ($J_{w,RO}$) was calculated using Eq. 2, where ρ is the density of the permeate (assumed to be water), and A' is the membrane active area. A and R were calculated using Eqs. 3 and 4, where c_P and c_F are the concentrations of the permeate and the feed solution. Finally, the salt flux coefficient (B) was estimated using Eq. 5, assuming a mass-transfer coefficient (k) of 1.07×10^{-5} m/s [26]. At least three samples were tested per degree of deformation (i.e., applied linear strain) for each membrane type. While direct-flow is not ideal for estimating the salt rejection, it allowed data collection and analysis of the two membranes at multiple values of linear strain within the project timeline.

$$J_{w,RO} = \frac{m_P}{t\rho_w A'} \quad (2)$$

$$A = \frac{J_{w,RO}}{\Delta P - \Delta\pi} \quad (3)$$

$$R = 1 - \frac{c_P}{c_F} \quad (4)$$

$$B = J_{w,RO}\frac{1-R}{R}\exp\left(-\frac{J_{w,RO}}{k}\right) \quad (5)$$

Osmotic water and salt flux through the TFC membranes in PRO mode (active layer facing the draw solution) were measured using a lab-built cross-flow apparatus described elsewhere [27]. These osmotic flux measurements were used to estimate the TFC membrane structural parameter (S). The apparatus uses a custom cell with two crossflow channels of 44 mm length, 14 mm width, and 2.35 mm depth, resulting in a membrane active area of 616 mm^2. It was used in countercurrent mode. Following a previous procedure, the membranes were contacted with a 50:50 (v/v) ethanol/water solution to wet the pores fully, followed by a thorough rinse with DI water, installation in the cell, and flooding of the feed channel with DI water to remove trapped air bubbles [27–29].

Four diamond-shaped spacers, two with 1.4 ± 0.1 mm opening size and two with 1.8 ± 0.1 mm opening size were used in the feed solution channel of the cross-flow membrane cell. The TFC membrane was placed directly on top of a spacer with smaller opening size. Draw solution (c_D = 0.6 M NaCl, 29.7 bar osmotic pressure at 25°C) and feed solution (DI water) were circulated through the membrane cell at equal flowrates of 1 LPM. The reservoir tanks held approximately 4.3 L of draw solution and 2 L of feed solution (V_{feed}). Five transmembrane pressures (ΔP) were tested: 12.5, 9.44, 5.94, 2.58, and 0.47 bar. The time period for each measurement (Δt) was 18 min starting when the rate of mass loss from the feed solution tank became constant (indicating steady state operation). Water mass loss from the feed solution tank (Δw_{water}) was recorded at each ΔP and used in Eq. 6 to calculate the osmotic water flux (J_w). Concurrently, the change in the conductivity of the feed solution tank (Δc_{feed}) was recorded and used in Eq. 7 to calculate the salt flux (J_s).

$$J_w = \frac{\Delta w_{water}}{A' \rho \Delta t} \quad (6)$$

$$J_s = \frac{V_{feed}\Delta c_{feed}}{A'\Delta t} \quad (7)$$

3. Results and Discussion

3.1 Effect of linear strain on TFC membrane properties

Figure 2a illustrates how the deformed TFC membranes were prepared using a tensile test apparatus. A sample of initial length (l_0) between clamps was stretched until the linear strain (ε_l, calculated using Eq. 8) reached a predetermined value (l_h at hold strain). Then, the sample was kept under constant stress for 5 min, which resulted in an increase of the sample length due to creep (l_m at maximum strain). Finally, the stress was released, and the sample contracted to its final length (l_f at the final strain). Since an initial tensile test revealed a strain-at-break of 20%, the hold strain values were varied from 1% to 15%. Figures 1b and c show typical results for SEAMAXX samples subjected to 15% and 1% hold strains. In Figure 2b, a yield point is observed at a stress of around 15 MPa and a strain around 2%; nevertheless, sample creep was observed below this yield point, as shown in Figure 2c.

$$\varepsilon_{l,i} = (l_i - l_0)\ /l_0 \times 100\% \quad (8)$$

Figure 2d shows the relationship between stress and strain at the hold point for the SEAMAXX and SW30XLE membranes. For both membrane samples there is a change in the slope of the stress-strain curves above 2% hold strain, suggesting they have similar strain-at-yield values. Above this yield point, both membranes show a linear stress-strain response. The Figure 2d insert shows a picture of SEAMAXX membrane coupons (active layer facing up in all cases) that were deformed by applying hold strains of 2%, 5%, 7% and 15%. It reveals a change in the coupon curvature for deformation above the yield point. This observation indicates that the porous support deformation is less reversible than that of the backing layer, after stress is

265 released. On the other hand, the stress at the maximum hold strain tested (15%) was just above
266 20 MPa for both membrane samples, which suggests that the membranes share similar backing
267 and porous support layer materials, given the similar mechanical behavior. Changes in transport
268 properties due to deformation, therefore, can be attributed to differences in the response of their
269 active layers to the applied strain.

270 Figures 2e and f show the effect of hold strain on values of maximum strain after a creep time of
271 5 min, and values of final strain for SEAMAXX and SW30XLE membrane samples. The
272 quotient of the maximum strain and the final strain was measured to be 1.49 for SEAMAXX and
273 1.79 for SW30XLE. This set of measurements suggests that during operation in PRO (membrane
274 under stress), TFC membranes can be deformed up to 79% greater than what is visualized upon
275 autopsy of a tested coupon. This finding is important for designing experiments to accurately
276 determine the burst point of the active layer upon pressure-induced deformation.

277 Figure S3 shows the effect of hold strain on the backing-free SEAMAXX membrane. In this
278 case, the quotient of the maximum strain and final strain at 10% hold strain was 1.45, like the
279 value obtained for the as-received membrane. However, during testing, 62% of the 10% hold
280 strain samples and 20% of the 5% hold strain samples failed during the test interval. The high
281 failure rates suggest that the backing-free structure is likely to break when subjected to constant
282 stresses close to its tensile strength.

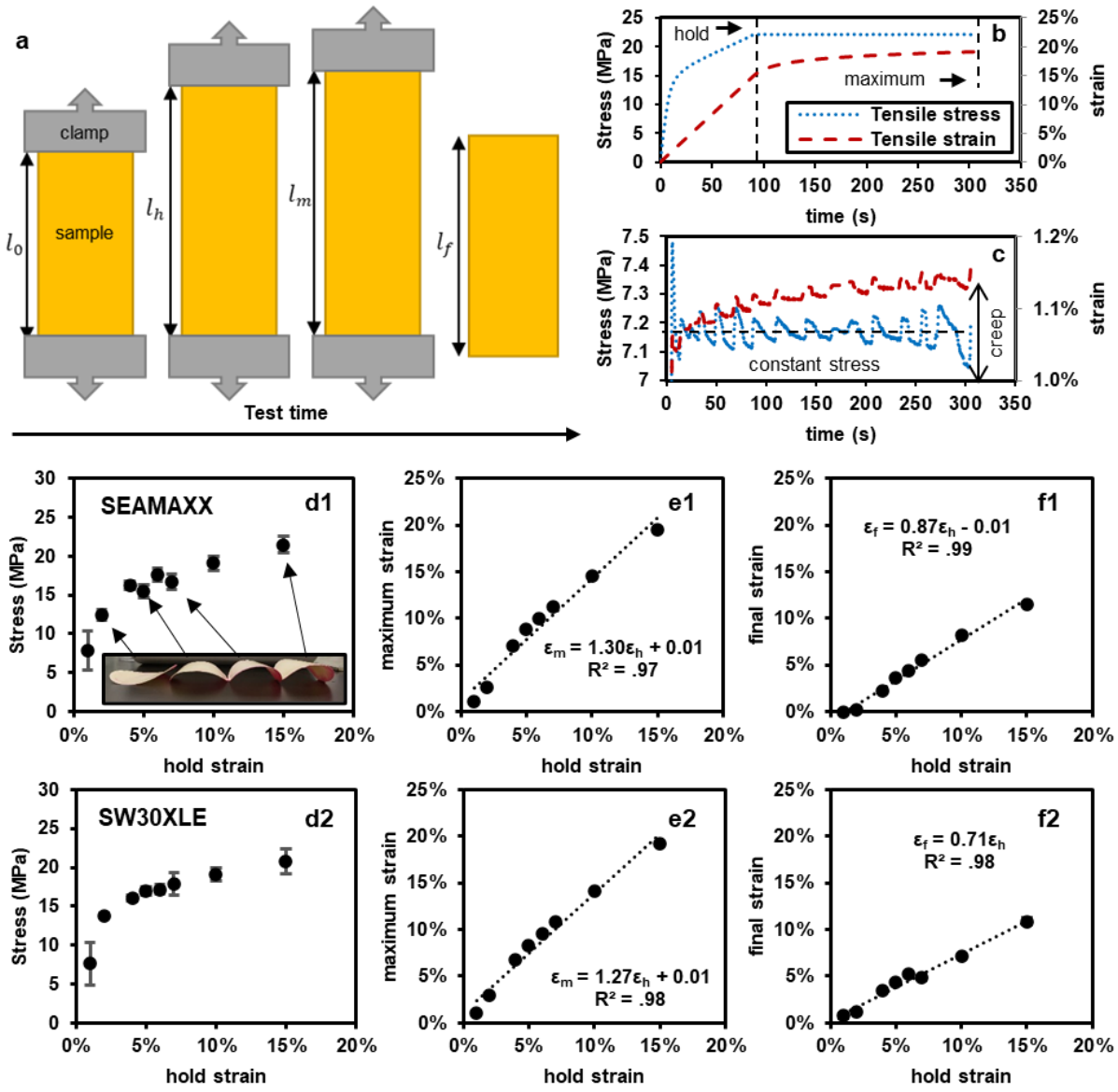

Figure 2. Schematic illustration of the method used to prepare deformed TFC membrane samples using a tensile test apparatus (a). Typical result of a creep test for a SEAMAXX sample subjected to a hold strain of 15% (b) and a 1% hold strain (c). Measured tensile stress (d), maximum strain after a creep time of 5 min (e), and final strain at different applied hold strains (f) during TFC membrane deformation tests. Numbers 1 and 2 denote SEAMAXX and SW30XLE samples. The insert in d1 shows a picture of membrane coupons that were deformed by applying hold strains of 2%, 5%, 7% and 15%.

Figure 3 shows the measured water permeance and salt flux coefficient for deformed SEAMAXX and (ethanol pre-treated) SW30XLE coupons with respect to the final strain. During these transport measurements, the membranes were supported on a flat, porous sintered steel

plate. Thus, no additional tensile strain was expected during testing. The transport properties of the SEAMAXX membrane were affected more by the applied strain than the SW30XLE membrane. Both water permeance and salt flux coefficient of SEAMAXX membranes increased up to 50% upon deformation compared to as-received membranes, which could be attributed to the thinning of the active layer and the creation of interchain volume in the active layer upon stretching. To visualize how strain changes the morphology of the active layer, we obtained SEM images of the tested SEAMAXX coupons. Figure 4 shows that upon increasing the applied strain, deformed (darker) areas appear on the surface of the active layer. The deformed areas on SEAMAXX grew perpendicularly to the direction of the stress, similarly to the crack sites reported by Stafford and coworkers when applying stress to polymer films and membranes [24]. However, we do not believe that the deformed areas are cracks since this would lead to a considerable increase in the salt passage through the membrane, which was not observed. Instead, we believe they are regions of stretched polyamide with lower resistance for transport of water and salt. Samples with the largest deformation (15% hold strain) formed salt crystals along the interfaces between the deformed and intact polyamide (after testing and drying). It could be expected that salt crystals would form on top of this interface if we assume that this interface has the highest passage of salt water. Although the salt rejection would be lower through these regions, a higher flux through them would lead to more severe concentration polarization and the possibility of salt precipitation.

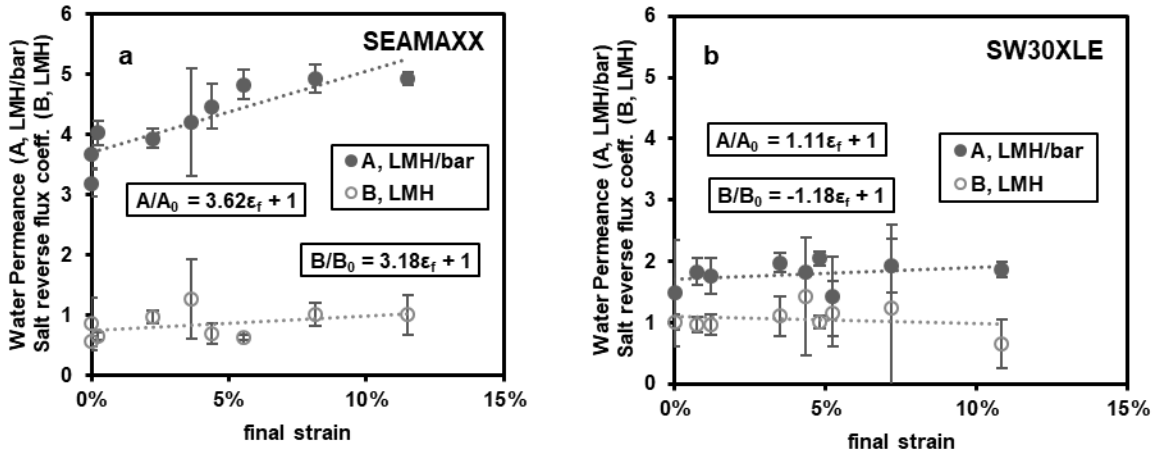

Figure 3. Dependences of water permeance and salt flux coefficient on final linear strain (degree of deformation).

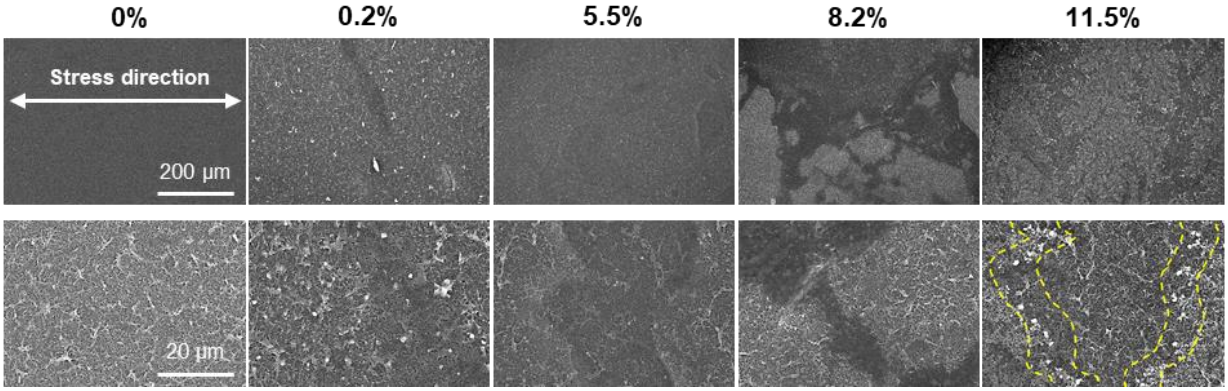

Figure 4. SEM micrographs of deformed SEAMAXX membranes following transport measurements. Samples with different final linear strain are shown. Stress direction and scale bars are common.

Conversely, the tighter SW30XLE membrane showed random variations in the measured transport properties upon deformation (Figure 3b) suggesting that this active layer is less susceptible to deformation. More interestingly, no break point (i.e., drastic increase in salt flux) was observed for SEAMAXX or SW30XLE up to final strains of 11% and 12%, respectively. Stafford and coworkers [24] measured the onset fracture strain of commercial crosslinked polyamide layers from a SWC4+ TFC membrane similar to the SEAMAXX and SW30XLE membranes. The reported average onset fracture strain was 14% (±4%) which is above the maximum final strain values for the membranes that we tested. Yet our maximum strains during

coupon preparation approached 20% (Figure 2e), above the reported onset fracture strain. Thus, we submit that active layers in the TFC membranes tested can recover in part from the onset of fracture upon the release of the stress (and consequent reduction of strain). To overcome the experimental challenge of measuring the burst strain of the polyamide layers without breaking the whole membrane structure (found to occur at an applied strain of 20%), we designed a burst pressure experiment that we describe in the following section.

3.2 Burst pressure and localized strain in TFC membranes

Wang et al. [23] reviewed the methods used for measuring the mechanical properties of membranes for water treatment. Among the reported properties was the burst pressure, which often is evaluated by pressurizing a membrane cell and, depending on the membrane configuration, recording: (1) the pressure when sudden change in conductivity occurs (hollow fibers) or (2) the pressure when the whole membrane breaks (Mullen burst test, flat sheets) [30]. The first method is more useful to relate mechanical properties with membrane performance since it determines the pressure at which the membrane loses its selectivity (transport failure), compared to the second method which measures a mechanical failure. We translated the first method to a flat sheet configuration to evaluate the burst pressure of flat sheet membranes by constructing the lab-built apparatus shown in Figure S2. Figure 5a shows representative examples of pressure and conductivity profiles during a burst pressure experiment for as-received and backing-free SEAMAXX membranes. The x-axis in Figure 5a has been normalized to have a similar time-to-burst (t_{burst}); however, this time was different in every experiment ranging from 15 h to 30 h for the as-received membranes and from 7 h to 82 h for the backing-free membranes. In Figure 5a the burst pressure is denoted as the maximum pressure reached

before a permanent change was observed in the slope of the conductivity versus time plot, denoted as t_{burst}, which was higher for the as-received membrane than the backing-free membrane.

Figure 5b shows the measured burst pressure for SEAMAXX as received and backing-free samples. The burst pressure was approximately 10 times higher for the membrane with the backing layer, which is expected since the role of the nonwoven backing is to provide mechanical stability to the TFC membrane structure. This result highlights an important, often overlooked point: burst pressure is not an intrinsic membrane property. The burst pressure depends on the structure supporting the membrane (typically spacers or carriers) during operation. For the case of the membranes studied in our osmotically-driven burst pressure cell, the membrane spans a 2.5 cm diameter opening, which is considerably larger than the opening sizes of spacers and carriers (around 1 mm). That is the reason for the relatively low burst pressures reported in the figure. Figure 5b also shows the membrane coupon maximum deflection, w_0, defined as the offset distance of the center of the test coupon from the original test plane. The as-received membrane showed a lower degree of deformation (i.e., deflection); however, values for w_0 were evaluated after testing when there was no applied stress on the membrane coupons. Since our creep tests showed that the as-received membranes can recover partially after stress is released, we believe that the actual strain-at-burst for the as-received membranes is higher than the measured final value. Also, given that the porous support is more susceptible to irreversible deformation than the backing layer, we hypothesize that the strain-at-burst of the as-received membrane would be closer to the measured value for the backing-free samples.

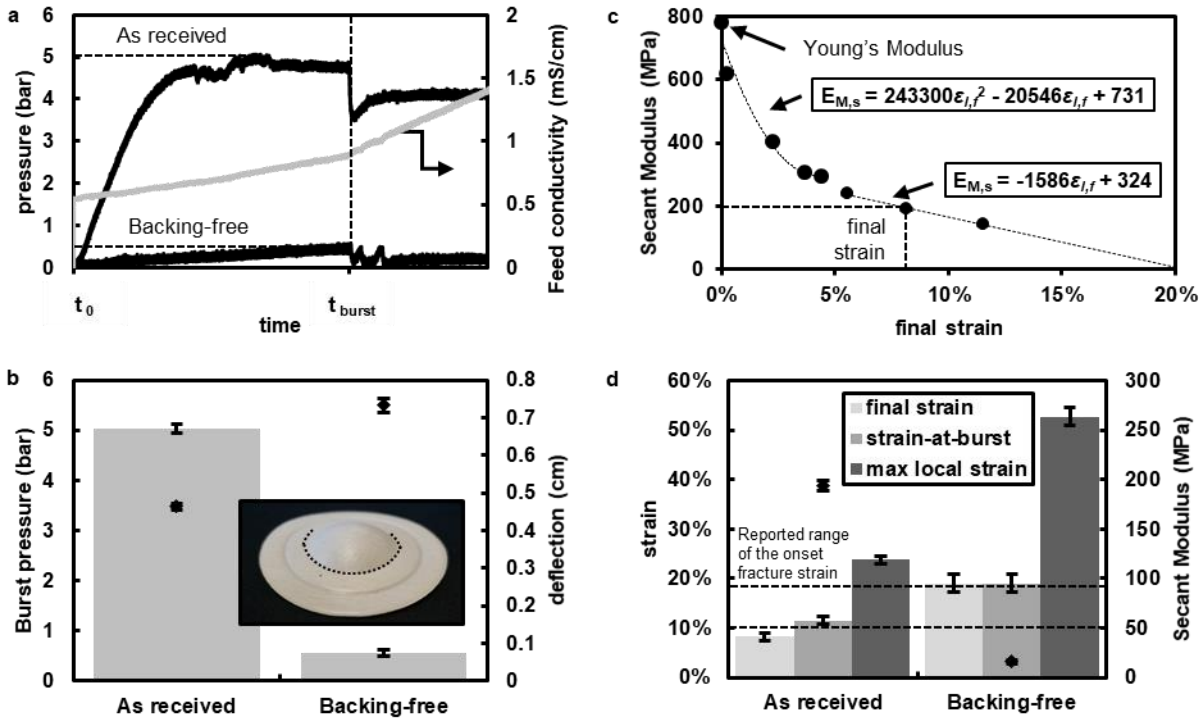

Figure 5. (a) Typical burst pressure test results. (b) Measured burst pressure (gray bars) and membrane coupon deflection (black diamonds) after burst pressure tests for SEAMAXX as-received and backing-free samples. The insert in b is a picture of a typical as-received membrane coupon after testing with the backing layer facing upward. Dotted line outlines the deformed testing area. (c) Secant modulus of the as-received SEAMAXX membrane. Dashed lines highlight the final strain measured from coupons tested for burst pressure and the corresponding secant modulus. Dotted lines show equation fits used to evaluate the secant modulus using the measured final strain. (d) Measured final strain, calculated strain and maximum local strain at burst (bars), and the observed secant modulus at burst (black diamonds). Dashed lines show the reported range of the onset fracture strain for the active layer of a TFC RO membrane [24].

The deflection of a thin membrane on top of a circular opening of radius R_M follows a parabolic profile (as shown in Eq. 9); and ΔP during the burst pressure testing can be estimated using Eq. 10 [31], where σ_0 is the residual stress on the membrane, E_M is the Young's Modulus of the membrane, v_M is the Poisson ratio of the membrane, and t_m is the membrane thickness.

$$w = -w_0\left(1 - \frac{x^2}{R_M^2}\right) \tag{9}$$

$$\Delta P = \frac{4w_0 t}{R_M^2}\left(\sigma_0 + \frac{2}{3}\frac{w_0^2}{R_M^2}\frac{E_M}{1.026-0.793\upsilon_M-0.233\upsilon_M^2}\right) \quad (10)$$

The term to the right of σ_0 is the stress induced to the membrane that leads to a deflection (σ_R), which we assumed to be considerably greater than σ_0. The Poisson ratio of porous materials approaches zero as the porosity increases [32,33]. Since the porosity of TFC membranes varies through the cross-section and can be as high as 60%, we assume that ν_M is 0, and we do not expect this value to be above 0.1. The thickness of the SEMAXX membrane was measured to be 154 ± 1 μm as received and 88 ± 2 μm when the nonwoven was removed. The Young's Modulus of the SEMAXX membrane as received was calculated to be 784 MPa from Eq. 11, where σ is the stress) from Figure 2d at the lowest hold strain (elastic region).

$$E_M = \frac{\sigma}{\varepsilon_{l,h}} \quad (11)$$

Substituting these values and the maximum deflection w_0 reported in Figure 5b into Eq. 10 gives an estimate of 18 bar for ΔP, which is considerably higher than the experimentally measured value of 5 bar. The reason for this discrepancy is that the application of Young's Modulus assumes that the material behaves elastically. The permanently deformed coupons provide contrary evidence to this assumption. The membranes deform irreversibly, i.e., the stress on the material during testing was higher than its yield strength. To account for this irreversible deformation, we propose to use a secant modulus, defined as the slope of the line that passes through the origin of the stress-strain curve and a second point on the stress-strain curve (Figure 2d). Secant modulus varies with strain and, therefore, must be defined based on the strain value that is used.

In Figure 5c the secant modulus is plotted with respect to the final strain. The estimated secant modulus at the final strain after burst pressure testing (8.2%) was estimated to be 194 MPa.

Applying this value and the experimentally measured burst pressure (5.0 bar), Eq. 10 was used to calculate an expected deflection of 0.55 cm (0.09 cm higher than the measured value). Since our creep tests showed that the as-received membranes can recover partially after stress is released, we expect that the deflection decreases slightly after removing the coupon from the testing apparatus. We therefore believe that the estimated deflection from Eq. 10 represents the strain-at-burst for the as-received SEAMAXX membrane. Figure 5d shows the measured final strain and calculated strain-at-burst of the SEAMAXX membrane (as received and backing-free). Since we showed that the backing-free membrane is likely to break during a period of constant stress close to it tensile strength (Section 3.1, Figure S3), it was assumed that the backing-free membrane does not recover from the deformed state; therefore, the measured value is the same as the estimated strain-at-burst. The calculated strain-at-burst for the as-received membrane was 40% higher than the measured final value, which agrees with our observation during our tensile creep tests (constant stress testing) that the final and maximum strain values differ up to 49% for the SEAMAXX membrane. Also, the estimated strain-at-burst for SEAMAXX samples fall within the range of the reported onset fracture strain of a polyamide layer from another commercial membrane [24]. However, the calculated strain-at-burst for the as received and backing-free membranes are different (at confidence interval of 95%), which suggests that, in the as received case, other factors can contribute to the failure of the membrane during the burst test.

To calculate the maximum strain subjected to a membrane coupon, we used local strain, which we defined in Eq. 12 as the relative differential change in length of the membrane (dx) due to a deflection (dw). The maximum local strain is calculated using Eq. 13 which is obtained by

436 substituting the derivative of Eq. 9 into Eq. 12 and evaluating it at the border of the circular
437 opening (i.e., $x = R_M$).

438 $$\varepsilon_{l,local} = \frac{\sqrt{dw^2+dx^2}-dx}{dx} \quad (12)$$

439 $$\varepsilon_{l,local,max} = \sqrt{\left(\frac{2w_0}{R_M}\right)^2 + 1} - 1 \quad (13)$$

440 Figure S4 shows the difference between the observed strain (average value) and the local strain.
441 Figure 5d shows that the maximum local strain can reach values above 20% at the border of the
442 opening, above the reported onset fracture strain, suggesting that this location of the membrane is
443 most susceptible to failure. Figure 5d also shows that the estimated secant modulus of the
444 backing-free membrane was 16 MPa, which was calculated from Eq. 10 using the measured
445 burst pressure and deflection. It has been reported for unsupported, porous polysulfone
446 membranes that the tensile strength ranges from 4.2 to 7.3 MPa, and the elongation at break from
447 20% to 25% with uncertainties of up to 18% [34–36]. We previously reported the tensile strength
448 of a backing-free SW30HRLE membrane to be 5.3 MPa [27]. For the SEAMAXX backing-free
449 membrane we measured its tensile strength to be 4.8 ± 0.1 MPa, and its elongation at break 24%
450 ± 3%. The secant modulus had its lowest value at the break point (see Figure 5c for example).
451 Using these reported values, the secant modulus at break would range from 17 MPa to 36 MPa.
452 We believe that our calculation of a secant modulus of 16 MPa for the backing-free membrane is
453 reasonable given the fact that the strain rate in the burst pressure experiment (test time > 7h) is
454 much slower than a tensile test (test time < 3 min), allowing the material to show stress
455 relaxation. Nonetheless, our observation supports the idea that the secant modulus and the

reported onset fracture strain [24], can be used with Eq. 10 to estimate the burst pressure of the TFC membrane for both the as-received and backing-free samples.

3.3 Introducing membrane deformation into boundary layer model

3.3.1 Measuring membrane deformation after PRO testing

After analyzing the deformation and burst pressure for membranes atop a large opening size (25.4 mm) and relating them to the membrane mechanical behavior (secant modulus), we used those findings to correlate the increased salt flux during PRO operation with the increased strain on the membrane due to deformation against the feed spacer. Initially, the PRO-tested membrane coupons were analyzed using LEXT, which allowed us to visualize and quantify the deformation of the membrane. Figure S1 compares representative LEXT images of tested membrane coupons to an as-received membrane. The images show that the membrane coupons were deformed irreversibly by compression against the wires of the feed spacer that supported them within the membrane cell. Similar to the burst pressure tests, the membrane coupons were subjected to stresses higher than the yield strength of the membrane and were deformed irreversibly. Additionally, dark areas were observed in the tested coupons, and generally appeared adjacent to the wire path (blue lines in Figure S1). This observation further supports the idea that higher deformation occurs along the border of the opening, which we postulated based on findings from the burst pressure experiments. This aligns with previous studies that incorporated membrane taping along the borders of the flow channels of membrane cells to avoid membrane deformation [37,38].

Figure 1 shows a 3D rendering of a tested membrane coupon based on measured height profiles, which were used to measure the deflection of the membrane. This measurement was done by selecting a membrane section spanning an opening and choosing a cross-sectional plane

perpendicular to the wire direction that had the largest deflection (w_0), also shown in Figure 1. Figure 6a presents an example deflection profile obtained using LEXT of a tested TFC membrane after osmotic flux measurements in PRO mode at a maximum pressure of 12.5 bar. When evaluating the change in deflection with distance (dw/dx), two deformation profiles appeared: one followed the shape of the wire, and the other followed a parabolic trajectory (like the coupons tested for burst pressure). The local strain profile was calculated using Eq. 12, which revealed a maximum strain of just below 4% at the border between the deformation profiles. Figure 6b shows the measured deflection and length of the parabolic profile measured with LEXT. The final average deflection measured after testing (i.e., after releasing the applied stress) was 110 μm ± 49 μm and the average length of the parabolic profile was 1.41 mm ± 0.16 mm, which is slightly longer than the measured opening size of 1.37 mm for the feed spacer. The measured final strain was 1.8%, the estimated strain evaluated at P_{max} (12.5 bar) using Eq. 14 [31] and the secant modulus (437 MPa) from Figure 5c was 10%, and the calculated maximum local strain was 29% at the border between the wire and parabolic profiles at P_{max}. These results reveal that the SEAMAXX membrane was deformed above the reported onset fracture strain; therefore, a loss in selectivity would be expected, which agrees with an increased salt flux observed during PRO testing with the cross-flow cell.

$$\Delta P = 13.6\frac{w_0 t}{a_M^2}\left(\sigma_0 + 1.61\frac{w_0^2}{a_M^2}\,\frac{E_M(1.446-0.427\nu_M)}{1-\nu_M}\right) \quad (14)$$

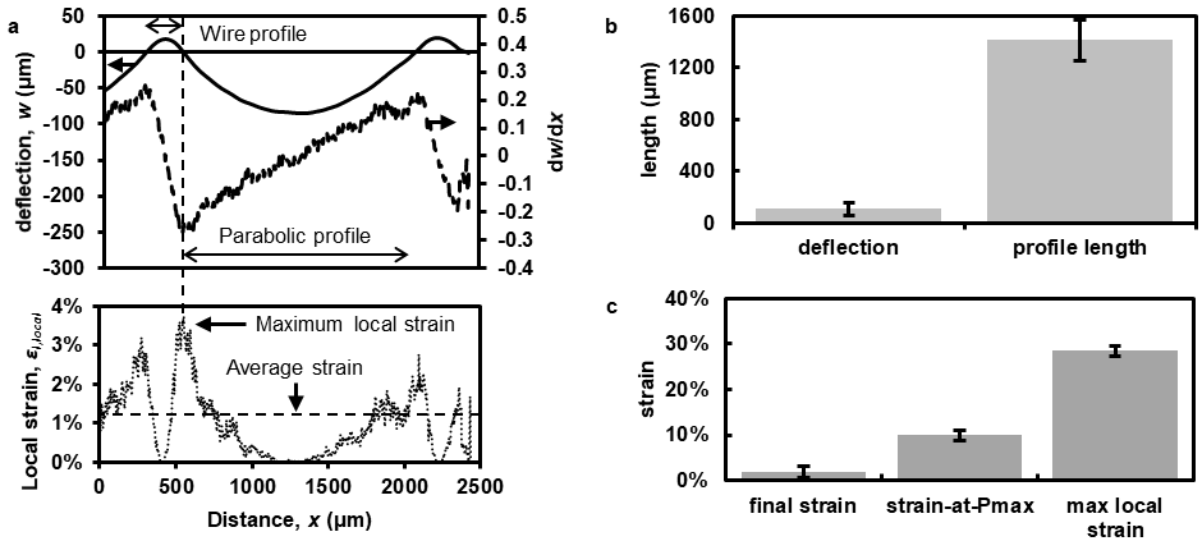

Figure 6. (a) Example of a deflection profile (taken at the maximum deflection) of a tested TFC membrane after osmotic flux measurements under PRO mode at a maximum pressure of 12.5 bar. (b) The final average deflection and the length of the parabolic profile. (c) Measured final strain, the estimated strain at P_{max} (12.5 bar), and the calculated maximum local strain at P_{max}. Values are for averages obtained using LEXT on a deformed SEAMAXX membrane on top of a feed spacer opening.

Figure 7a,b shows the experimental results (symbols) for osmotic water flux (J_w) and selectivity (J_s/J_w) in PRO mode at different transmembrane pressures for the SEAMAXX and SW30XLE membranes. The water flux followed the expected decreasing trend with increasing transmembrane pressure; however, salt flux showed an unpredicted, but commonly reported, increasing trend. With the goal of improving the predictive modeling of the salt flux dependence with pressure during PRO operation, we developed a boundary layer model that is based on a conventional model [16]. This model relates the deformation of the membrane (defined as linear strain) with the transmembrane pressure by using the mechanical properties of the membrane and the spacer characteristics, and following the observations obtained from our mechanical property tests (Sections 3.1 and 3.2).

3.3.2 Defining strain as function of pressure

The deflection (w) of a membrane on top of an opening follows a parabolic profile [31]. The deflection in terms of the position along the axis parallel to the spacer opening (x) is defined in Eq. 15.

$$w = w_0\left(1 - 4\frac{x^2}{a_M^2}\right) \tag{15}$$

w_0 is the maximum deflection and a_M is the spacer opening size. The length of the membrane after deformation (l_f) can be calculated as the arc length of Eq. 15 along the opening size as shown in Eq. 16. Then, the linear strain (ε_l) on the membrane can be calculated using Eq. 17.

$$l_f = \int_{-a_M/2}^{a_M/2}\sqrt{1 + \left(\frac{dw}{dx}\right)^2}\,dx \tag{16}$$

$$\varepsilon_l = \frac{l_f - a_M}{a_M} = \frac{1}{2}\left(\frac{\sinh^{-1}\left(\frac{4w_0}{a_M}\right)}{\frac{4w_0}{a_M}} + \sqrt{\left(\frac{4w_0}{a_M}\right)^2 + 1}\right) - 1 \tag{17}$$

For a thin membrane ($t/w_0 < 1$), the hydrostatic pressure applied (ΔP), and the stress felt by the membrane ($\sigma_m = \sigma_0 + \sigma_a$) on top of a square opening (of opening size a_M) are related by Eq. 18. If we assume that the residual stress (σ_0) is considerably smaller than the stress generated by the deflection (σ_a, term on the right side in parentheses), then the ratio $4w_0/a_M$ can be written as in Eq. 19.

$$\Delta P = 13.6\frac{w_0 t}{a_M^2}\left(\sigma_0 + 1.61\frac{w_0^2}{a_M^2}\,\frac{E_M(1.446 - 0.427\nu_M)}{1-\nu_M}\right) \tag{18}$$

$$\frac{4w_0}{a_M} = 1.43\left[\frac{a_M}{t}\,\frac{1-\nu_M}{E_M(1.446 - 0.427\nu_M)}\right]^{1/3}\sqrt[3]{\Delta P} = K\sqrt[3]{\Delta P} \tag{19}$$

Finally, Eq. 20 relates the strain (ε_l) and ΔP. Also, we introduce a "deformability" coefficient K, defined in Eq. 21, where a_M is the opening size of the spacer. Note that K is independent of strain if the material behaves elastically. However, if the stress exceeds the yield point, then E_M becomes the secant modulus (instead of the Young's Modulus), which depends on the strain of the membrane.

$$\varepsilon_l = \frac{1}{2}\left(\frac{\sinh^{-1}\left(K\sqrt[3]{\Delta P}\right)}{K\sqrt[3]{\Delta P}} + \sqrt{\left(K\sqrt[3]{\Delta P}\right)^2 + 1}\right) - 1 \tag{20}$$

$$K = 1.43\left[\frac{a_M}{t}\frac{1-\nu_M}{E_M(1.446-0.427\nu_M)}\right]^{1/3} \tag{21}$$

3.3 Other membrane deformation associated factors

Membrane deformation also leads to an increase in surface area above the projected (or initial) membrane testing area (A'_0). This change in surface area occurs mainly on the membrane regions atop of the spacer openings and, therefore, will depend on the relative open area of the feed spacer (OA) reported by the manufacturer. Eq. 22 shows an expression to calculate the surface area during the experiment, based on the membrane surface strain ($\varepsilon_{A'}$). The surface strain depends on pressure and the deformability coefficient according to Eq. 23.

$$A' = A'_0(1 + \varepsilon_{A'}) \tag{22}$$

$$\varepsilon_{A'} = OA\left(\frac{2}{3}\frac{\left(\left(1+\left(K\sqrt[3]{\Delta P}\right)^2\right)^{3/2}-1\right)}{\left(K\sqrt[3]{\Delta P}\right)^2} - 1\right) \tag{23}$$

We also considered changes in the structural parameter (S) upon compression, which we describe in the Supporting Information. Eq. 24 expresses the structural parameter dependence on

transmembrane pressure. In this equation, subscript 0 indicates initial (pre-deformation) values.

$$S = S_0\varphi_0\left(\frac{1+\varepsilon_{A'}}{\varphi_0+\varepsilon_{A'}}\right)\frac{1-\frac{\Delta P}{E_r}}{1-\left(\frac{1+\varepsilon_{A'}}{\varphi_0+\varepsilon_{A'}}\right)\frac{\Delta P}{E_r}} \quad (24)$$

The initial structural parameter can be evaluated with osmotic water flux measurements ΔP=0 [29], or estimated using the definition of intrinsic structural parameter. The initial porosity can be measured gravimetrically by fluid displacement [39], mercury intrusion porosimetry, or x-ray microscopy [40]. The latter method was used to measure the porosity of commercial TFC membranes and generated φ_0 values of 35% ± 2% for BW30 and 43% ± 1% for SW30XLE [40]. We used an initial porosity, φ_0, of 39% for our estimations. The compressive reduced modulus, E_r, can be obtained by measuring the relative change in thickness of the membrane when applying compressive stress [39]. We determined E_r for the SEAMAXX membrane by measuring the relative change in thickness of the membrane when applying compressive stress using a two-stage penetration test as described elsewhere [39]. We measured this value to be between 16 and 24 MPa for the as received membrane and between 11 and 21 MPa for the backing-free membrane at a maximum compressive stress of 1.8 MPa (see Figure S5). We selected an E_r value of 20 MPa for the calculation of S.

3.3.4 Deriving the solution-diffusion model with defects

Based on our observation that the average strain of the membrane after PRO testing (~ 2%) is well below the reported onset fracture strain (14% ± 4%) and the strain-at-burst that we measured via burst pressure testing (~ 11%), we hypothesize that the failure mechanism during PRO testing is due to local strain and thus localized defect formation, rather than global or average changes in the membrane transport properties. This idea is consistent with data presented in Figure 3; in the expected range of strain, the dependence of the transport properties (A and B)

on strain is negligible. Instead, we believe that the increased salt passage is caused by the formation of non-selective defect sites and is proportional to the local maximum strain ($\varepsilon_{l,local,max}$, see Eq. 25). These defect sites allow a pressure-driven flow of water and accompanying salt in the direction opposite to the osmotic water flux (in the case of PRO). Eqs. 26 and 27 are used to estimate water and salt flux through defect sites.

$$\varepsilon_{l,local,max} = \sqrt{\left(K\sqrt[3]{\Delta P}\right)^2 + 1} - 1 \quad (25)$$

$$J_{w,\text{defect}} = -K_A \varepsilon_{l,local,max}(A\Delta P) \quad (26)$$

$$J_{s,\text{defect}} = J_{w,\text{defect}} c_D \quad (27)$$

K_A is a correction factor to estimate the water permeance of the defect site relative to the membrane water permeance (A). Note that the effective water permeance across defects would be the product between K_A and A. We chose to make use this notation to compare the relative difference between the membrane and the estimated defect site water permeances. Previously, Pinnau and coworkers [6] proposed a solution-diffusion model that accounts for defects in the selective layer by including the flux through such defects. In their work, the magnitude of this flux was attributed to the convective flow permeability coefficient as a characteristic of the selective layer. We submit that the flux through defects is a combination of factors that include the permeance of the active layer, as well as the deformability of the TFC membrane structure.

Finally, we propose a boundary layer model to describe the water and salt flux through a membrane in an osmotic process (Eqs. 28 and 29) that includes aspects of membrane deformation. In these equations, subscripts D and F stand for values of the draw and feed solutions, respectively. π is the osmotic pressure, c is the molar concentration of the salt, k is the

mass-transfer coefficient, D is the salt diffusion coefficient in water (assumed to be 1.6×10^{-9} m^2/s [41]). A conventional boundary layer model used in previous PRO studies [16,42,43] can be obtained from Eqs. 28 and 29 by setting $\varepsilon_{A'}$ and ε_l to zero and using S as a fitting parameter. In our case, the structural parameter was evaluated at the lowest transmembrane pressure (i.e., low deformation, S_0), and the defect site water permeance correction factor K_A is a fitting parameter. The benefit of our model is that the physical meaning of our fitting parameter (pressure-driven flow factor) is in accordance to the experimental observation (increased salt flux). In contrast, attributing an increased salt passage to an increased structural parameter is not correct since a larger structural parameter would decrease the effective concentration gradient at the active layer surfaces, reducing the observed salt flux. Figure S6 presents the algorithm used to fit the model Eqs. 28 and 29 to experimental data.

$$J_w = (1 + \varepsilon_{A'})A\left\{\frac{\pi_D \exp(-J_w/k) - \pi_F \exp(J_w S/D)}{1 + B/J_w[\exp(J_w S/D) - \exp(-J_w/k)]} - \Delta P\right\} - K_A \varepsilon_{l,local,max}(A\Delta P) \quad (28)$$

$$J_s = (1 + \varepsilon_{A'})B\left\{\frac{c_D \exp(-J_w/k) - c_F \exp(J_w S/D)}{1 + B/J_w[\exp(J_w S/D) - \exp(-J_w/k)]}\right\} + K_A \varepsilon_{l,local,max}(A\Delta P)c_D \quad (29)$$

Figure 7 shows the experimental osmotic water flux and selectivity results measured in PRO for the SEAMAXX and SW30XLE membranes. As expected, there was higher salt flux for both membranes when testing at high pressure; in fact, the salt flux was 5 (SEAMAXX) and 10 (SW30XLE) times higher when comparing the values at the highest and lowest testing pressure. Figure 7 also shows the results of fitting the conventional model [16,43,44] (labeled "NO deformation" in Figure 7, dotted curves) and our model, which includes changes in the water flux due to increased strain. The goodness of fit was improved particularly in the selectivity of the membranes. The relative-root-mean-square-error (RRMSE) changed from 8.3% to 5.3% for SEAMAXX and from 4.7% to 10.3% for SW30XLE in the case of water flux, which means

good fits were obtained for both models (RRMSE < 20%, [45]). In the case of salt flux, the RRMSE was decreased from 83.3% to 17.2% for SEAMAXX and from 61.9% to 9.1% for SW30XLE. The marked improvement in fit is due to incorporation of a pressure-dependent salt flux in our model. The fitted results were obtained using a water permeance correction factor, K_A, of 1.58 for SEAMAXX and 2.33 for SW30XLE. We also fitted our experimental data to our model while assuming no change in surface area (i.e. $\varepsilon_A = 0$) and a constant structural parameter (i.e. $S=S_0$ at any ΔP), and obtained K_A values of 1.60 for SEAMAXX and 2.34 for SW30XLE, which are very close to the ones obtained with the full model. This finding suggests that the most relevant factor, among the three studied, is the presence of defects.

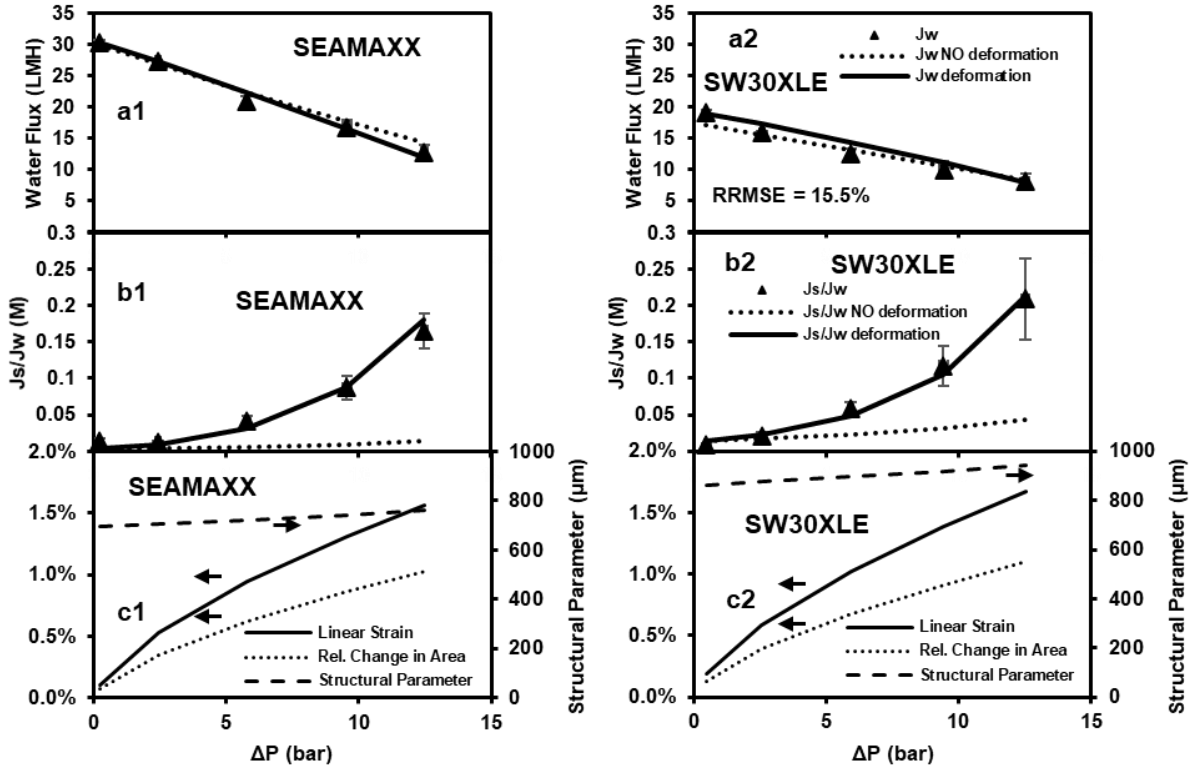

Figure 7. (a) Osmotic water flux and (b) selectivity results in PRO mode for the (1) SEAMAXX and (2) SW30XLE membranes at different transmembrane pressure (ΔP) values. (c) Modeling results of the change in linear strain, relative change in surface area, and structural parameter of the membranes at different transmembrane pressure.

Figure 7c shows the predicted changes in linear strain, relative change in surface area, and structural parameter as pressure increases. Both the change in linear strain and change in area were below 2.5%, which suggests that the decreased selectivity may be due to local defects, and that the increase in surface area does not play a significant role in the observed salt passage. Additionally, the predicted changes in the structural parameter were below 60 μm (less than 10%) at the maximum pressure. This finding suggests that even though there is a reduction of porosity (increased structural parameter), this compaction does not yield a considerable decrease in water flux through the membrane. Finally, our model suggests that among the different membrane deformation factors included, the most significant factor in the increase of salt passage in PRO operation is the formation of localized defect sites. With the goal of validating our observations, we used our model and fitting algorithm to estimate the membrane deformation in a number of reported PRO experiments, and used these observations to elucidate the typical tradeoff between mechanical deformation and support mass-transfer resistance in OP, particularly PRO.

3.4 Deformation model applied to other PRO experiments

Table 1 compiles information on PRO experiments reported in the literature that were used to validate our model. These reports included data for water and salt flux for at least four different pressure values and included characterization of their *A* and *B* parameters. In all these experiments, the feed solution had a concentration ≤ 0.01 M NaCl and draw solution concentration ≥ 0.5 M NaCl. Other experimental characteristics like the relative open area and opening size of the feed spacer; thickness, tensile strength, and Young's Modulus of the membrane; and active area and mass-transfer coefficient of the membrane cell were extracted from the papers as reported, estimated from reported data (e.g., mass-transfer coefficient from

crossflow velocity and crossflow channel dimensions), or assumed to be equal to data reported elsewhere using the same membrane or the same experimental setup. Among these characteristics, the mechanical properties of the membrane were reported least often, followed by the feed spacer dimensions, and the membrane thickness. As defined in the deformability coefficient (Eq. 21), all these characteristics contribute to the susceptibility of a membrane to deformation during PRO operation. Therefore, we strongly suggest that reports of future OP experimental work should include these characterization data.

Figure 8a shows the deformability coefficient calculated from the data collected in Table 1 for reported PRO experiments. Notably, we used the reported Young's Modulus in these calculations. The resulting deformability coefficients generally were lower for membranes tested on top of permeate carriers compared to those on top of diamond shaped spacers due to the smaller opening size of the former. The exception is the PEI set of membranes from [25], which did not have a backing layer and therefore are more susceptible to deformation. However, many of the references indicated that the membranes deformed irreversibly from PRO testing. Using the secant modulus would yield a better estimation of the extent of the membrane deformation in such cases, since the membranes did not deform elastically. Unfortunately, a stress-strain curve from tensile testing of the membrane is needed to estimate the secant modulus. Additionally, since the deformation is expected to be larger for membranes supported on diamond shaped spacers, the actual value of the deformability coefficient would be even larger for these cases when using the secant modulus.

To verify that our calculation method yields realistic values, we estimated the relative tensile stress on the membrane at the maximum testing pressure, defined as the quotient of the stress on the membrane that generates the membrane deflection (σ_R) and the tensile strength (stress-at-

676 break) reported in Table 1. Figure S7 shows that, based on our calculations, no membrane was
677 stressed past the break point. This finding is consistent with the literature; no membrane failures
678 were reported in these studies. The highest relative stress estimations were obtained for
679 membranes with thicknesses below 100 μm or those on top of spacers with an opening size
680 larger than 2.0 mm. Membranes on top of permeate carrier are estimated to be subjected to a low
681 tensile stress relative to their break point.

682 Table 1. Summary of the PRO experiments used to develop the model

Name	Membrane Provider	Type	Feed spacer type	Spacer Relative open area	Spacer Opening size (mm)	Membrane thickness (mm)	Tensile Strength σ* (MPa)	Young's Modulus E_M (MPa)	Water Permeance A (LMH/bar)	Salt Flux Coeff. B (LMH)	Active area (cm^2)	Mass transfer coefficient ($\times 10^{-5}$ m/s)	Ref.
SW30XLE	DuPont	TFC	Diamond shaped	0.44 [a]	1.37	0.140	23	761	1.49	0.97	6.16	3.44 [b]	This work
SEAMAXX	DuPont	TFC	Diamond shaped	0.44 [a]	1.37	0.154	28	784	3.83	0.54	6.16	3.44 [b]	This work
CTA-NW	HTI	CTA	Diamond shaped	0.55 [46]	2.60 [46]	0.144 [47]	54 [c] [48]	287 [c] [48]	0.44	0.07	140.00	1.17	[49]
CTA-W	HTI	CTA	Diamond shaped	0.55 [46]	2.60 [46]	0.045 [47]	41 [48]	604 [48]	0.37	0.28	140.00	1.17	[49]
CTA-P	HTI	CTA	Diamond shaped	0.55 [46]	2.60 [46]	0.045 [47]	41 [48]	604 [48]	0.75	0.63	140.00	1.17	[49]
2.0M	HTI	CTA	Permeate carrier	0.35 [14]	0.35 [d] [14]	0.052 [48]	41 [48]	604 [48]	0.61	0.47	138.7	3.24	[20]
1.5M	HTI	CTA	Permeate carrier	0.35 [14]	0.35 [d] [14]	0.052 [48]	41 [48]	604 [48]	0.61	0.47	138.7	3.24	[20]
1.0M	HTI	CTA	Permeate carrier	0.35 [14]	0.35 [d] [14]	0.052 [48]	41 [48]	604 [48]	0.61	0.47	138.7	3.24	[20]
0.5M	HTI	CTA	Permeate carrier	0.35 [14]	0.35 [d] [14]	0.052 [48]	41 [48]	604 [48]	0.61	0.47	138.7	3.24	[20]
S#1	HTI	CTA	Diamond shaped	0.69	2.95	0.052 [48]	41 [48]	604 [48]	1.37	1.00	140.00	6.91	[14]
S#2	HTI	CTA	Diamond shaped	0.55	2.60	0.052 [48]	41 [48]	604 [48]	1.37	1.40	140.00	6.91	[14]
S#3	HTI	CTA	Permeate carrier	0.35	0.35	0.052 [48]	41 [48]	604 [48]	0.95	1.00	140.00	6.91	[14]
PEI-1	Lab-made	TFC	Permeate carrier	0.35	0.35 [d] [14]	0.067	5.3 [e]	107	2.28	0.67	34.00	6.91 [f]	[50]
PEI-2	Lab-made	TFC	Permeate carrier	0.35	0.35 [d] [14]	0.076	5.3 [e]	150	2.09	0.87	34.00	6.91 [f]	[50]
PEI-3	Lab-made	TFC	Permeate carrier	0.35	0.35 [d] [14]	0.083	5.3 [e]	201	1.65	0.75	34.00	6.91 [f]	[50]
HTI-TFC 3.0M	HTI	TFC	Permeate carrier	0.64 [g]	0.35 [d] [14]	0.112 [48]	54 [48]	287 [48]	1.63	1.42	124.00	1.52 [b]	[38]
HTI-TFC 2.0M	HTI	TFC	Permeate carrier	0.64 [g]	0.35 [d] [14]	0.112 [48]	54 [48]	287 [48]	1.63	1.42	124.00	1.52 [b]	[38]
HTI-TFC 1.0M	HTI	TFC	Permeate carrier	0.64 [g]	0.35 [d] [14]	0.112 [48]	54 [48]	287 [48]	1.63	1.42	124.00	1.52 [b]	[38]
TFC-T	Lab-made	TFC	Diamond shaped	0.55	2.60	0.510	12	68	1.30	1.82	33.15	6.91 [f]	[46]

TFC-N	Lab-made	TFC	Diamond shaped	0.55	2.60	0.450	9	65	1.30	1.82	33.15	6.91 [f]	[46]
TFC-W	Lab-made	TFC	Diamond shaped	0.55	2.60	0.440	35	92	1.30	1.82	33.15	6.91 [f]	[46]
TNC-1	Lab-made	TFC	Diamond shaped	0.43 [a]	1.14 [51]	0.045 [h]	17	113 [i]	1.23	0.28	140.00	2.13	[52]
TNC-2	Lab-made	TFC	Diamond shaped	0.43 [a]	1.14 [51]	0.045 [h]	17	113 [i]	3.82	1.19	140.00	2.13	[52]
TNC-3	Lab-made	TFC	Diamond shaped	0.43 [a]	1.14 [51]	0.045 [h]	17	113 [i]	5.31	3.86	140.00	2.13	[52]
HTI	HTI	CTA	Diamond shaped	0.48 [a]	2.03 [53]	0.052 [48]	41 [48]	604 [48]	0.66	0.44	19.35	2.30 [b,j]	[54]
pTFC	Lab-made	TFC	Diamond shaped	0.48 [a]	2.03 [53]	0.070	9 [k]	65 [k]	5.30	4.97	19.35	2.30 [b,j]	[54]
mTFC	Lab-made	TFC	Diamond shaped	0.48 [a]	2.03 [53]	0.070	9 [k]	65 [k]	2.83	0.44	19.35	2.30 [b,j]	[54]
Toray-PRO	Toray	TFC	Permeate carrier	0.585 [g]	0.35 [d] [14]	0.160	25 [l]	770 [l]	3.12	0.54	20.02	2.56 [b,m]	[12]
HTI-FO	HTI	CTA	Permeate carrier	0.585 [g]	0.35 [d] [14]	0.100	54 [48]	287 [48]	0.72	0.41	20.02	2.56 [b,m]	[12]

[a] Calculated from ASTM-E11-17 from opening size and wire diameter [55]
[b] Calculated using the method described elsewhere [56]
[c] Assumed to be similar to the values for HTI-TFC since the backing layer is nonwoven for both
[d] Assumed to be similar to previously reported values for RO permeate carriers
[e] Assumed to be similar to previously measured strength for porous support made via phase inversion [27]
[f] Assumed to be equal to previously reported values from the same lab [14]
[g] Reported as void volume
[h] Estimated from reported scanning electron microscopy image
[i] Calculated as secant modulus at the break point
[j] Assumed a squared membrane area
[k] Assumed from previously reported fiber mats made via electrospinning from the same authors [53]
[l] Approximated based on our measurements for SW30XLE and SEAMAXX (TFC membranes with nonwoven backings and porous supports made via phase inversion)
[m] Assumed a crossflow velocity of 0.25 m/s

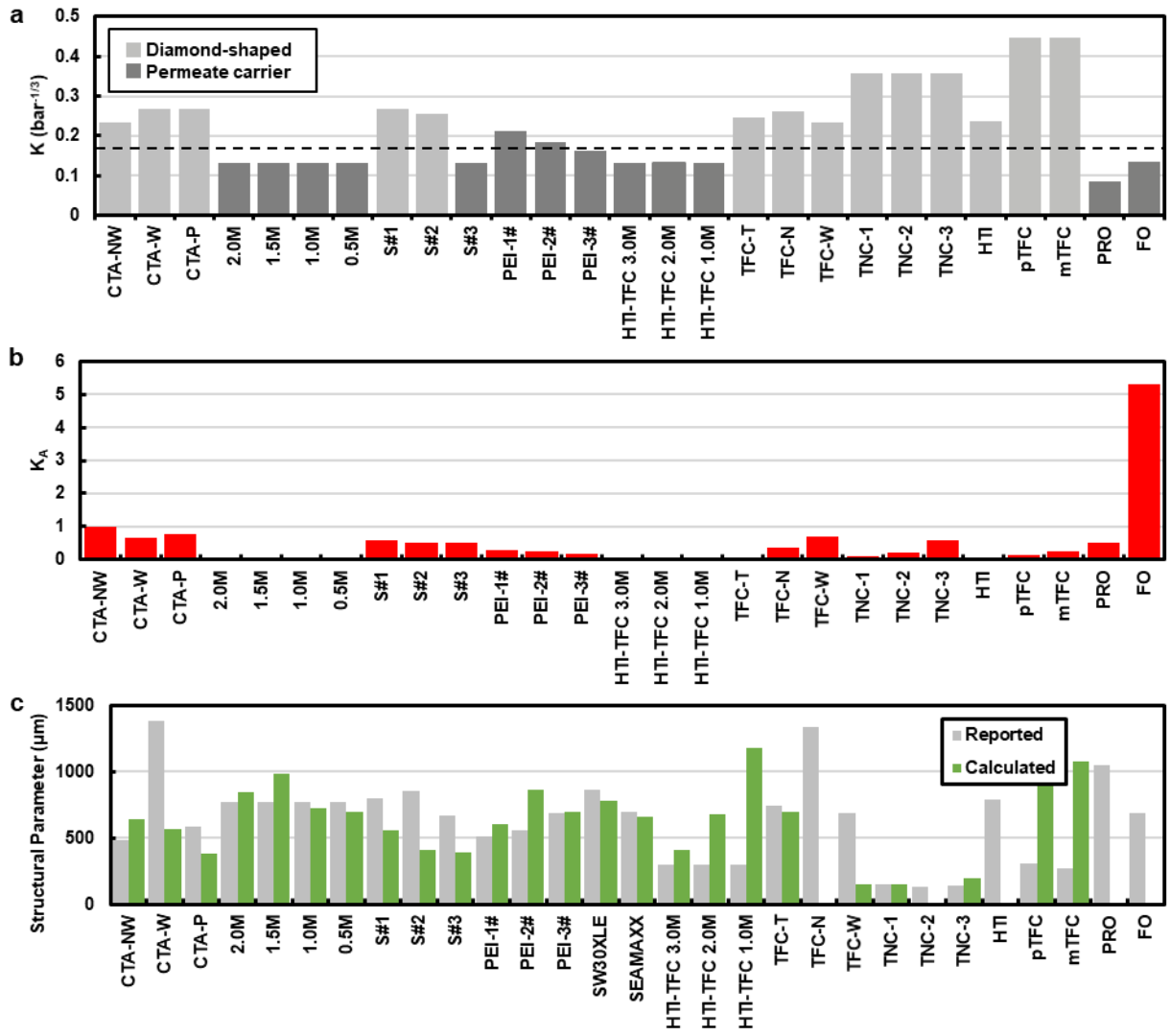

697

698 Figure 8. (a) Deformability coefficient calculated from the data collected in Table 1. Dashed line
699 shows the value for the SEAMAXX membrane used in this work. (b) Fitting results of the defect
700 site water permeance correction factor K_A. (c) Structural parameter calculated at the lowest
701 reported testing pressure and reported in each PRO experiment in Table 1.

702

703 Next, we applied our model Eqs. 28 and 29 to fit the experimental results of water and salt flux.
704 Figures S9 to S11 show the experimental data and the model fits. Figure 8b shows fitting results
705 of the defect site water permeance correction factor K_A. The average among the correction factor
706 values fitted was 0.55 (median = 0.24), which suggests that our current model may overestimate

the water permeance across the defect sites, assuming that defect sites have a higher permeance than the intact membrane. Additionally, seven PRO experiments, which all used permeate carriers as feed spacers, had a correction factor of exactly 0, which suggests that permeate carriers help to avoid defects. Nevertheless, one PRO experiment (labeled “FO”) in which a permeate carrier was used showed the largest correction factor, which suggests severe membrane deformation. We also compared these fitting parameter results to those calculated when the surface area and the structural parameter are kept constant. Figure reveals that results are similar to those when the variables change with pressure (Figure 8b).

Next, we compared our estimation of the structural parameter (obtained at the lowest reported test pressure) and the reported structural parameter in each case (Figure S12 shows the change in structural parameter with pressure in each case). In some cases, the calculated structural parameter was zero, which means that the measured water flux was above the maximum water flux attainable using the given mass-transfer coefficient, i.e., the external mass-transfer resistance accounted for all the reduction in driving force in the model. More interestingly, nearly all membranes tested on diamond shaped feed spacers showed a calculated structural parameter lower than the reported value. This means that the conventional methodology could lead to an overestimation of the structural parameter, since it would not only account for the internal mass-transfer resistance of the membrane, but also the reduced water flux due to membrane deformation. Figure S13 shows the structural parameter calculated at each pressure using the conventional boundary layer model. Generally, the calculated structural parameter increases as pressure increases (i.e. increased salt passage when deformation occurs), suggesting that the average value is higher than that evaluated at low pressure values. On the other hand, in the majority of cases, membranes with backing layers on top of permeate carriers showed a

730 higher calculated structural parameter than the reported value. This outcome is explained by the
731 fact that a dense backing layer like a permeate carrier, does not allow convective flow within its
732 structure, becoming an additional resistance layer for diffusion of solutes, increasing the
733 observed structural parameter. These observations constitute the tradeoff between mechanical
734 deformation and the mass-transfer resistance observed in pressurized OP such as PRO.

735 To further visualize the tradeoff between mechanical deformation and the mass-transfer
736 resistance in the PRO experiments studied, we defined metrics for each of these factors and
737 correlated them to the estimated maximum local linear strain for each experiment listed in Table
738 1. The mechanical deformability of the membrane was evaluated by calculating the change in
739 salt flux from the lowest to the highest testing pressure, normalized by the maximum applied
740 transmembrane pressure (ΔP_m) and the difference in the NaCl bulk concentration ($\Delta c = c_D - c_F$).
741 The mass-transfer resistance of the spacer was estimated using a residual structural parameter,
742 defined as the difference between the calculated structural parameter (green bars in Figure 8c)
743 and the intrinsic structural parameter of the membrane evaluated using the reported thicknesses
744 in Table 1 and previously measured values of porosity (φ_0=39%) and tortuosity (τ=1.26) [40].
745 Figure 9 shows the normalized change in water flux and the residual structural parameter (i.e., $S - t_0\tau/\varphi_0$)
746 with respect to the maximum local linear strain calculated using the deformability
747 coefficient. The data reveal that as the deformation increases, the salt passage through the
748 membrane increases as a result of decreased mechanical stability. However, increased
749 deformation also results in a lower mass-transfer resistance. Membranes supported in permeate
750 carriers mostly showed a lower salt passage and higher residual structural parameter compared to
751 ones on top of diamond shaped spacers. Residual structural parameters were as high as 1 mm.
752 Given that most of the reported membrane structural parameters were below 1 mm, residual

structural parameters of ≥1 mm suggest that permeate carriers can exacerbate the mass-transfer resistance in PRO operation. From the pool of references studied, the tricot-supported, fabric-reinforced TFC-T and the SiO2/PAN nanofiber supported TNC-1 membrane showed both high mechanical stability and low mass-transfer resistance, which supports the idea that mechanically-reinforced membranes are beneficial for OP such as PRO. Such reinforcement would enable the use of diamond or other spacer shapes that do not add to the overall mass-transfer resistance during operation. Finally, the deformability coefficient coupled with the transport properties can be used to determine the suitability of membranes for OP, especially pressurized operations like PRO.

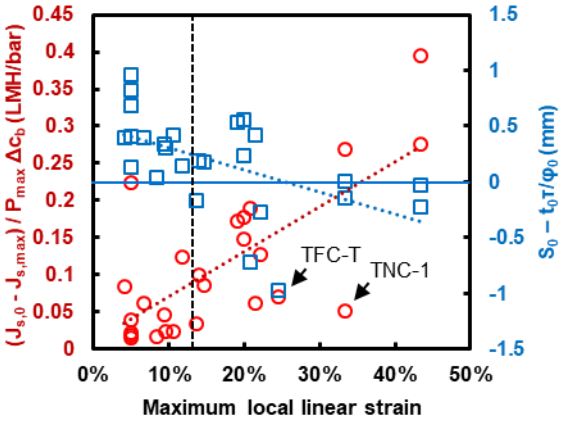

Figure 9. Normalized change in water flux and the residual structural parameter with respect to the maximum local linear strain for each experiment reported in Table 1, excluding TNC-3 and HTI-FO. The salt flux at the maximum pressure of the TNC-3 and HTI-FO membranes (see Table 1) was reported to be 18 and 30 mol/m^{2}h, respectively. These values are considerably higher than the next highest value, 4.5 mol/m^{2}h for TFC-W; therefore, they were considered exceptional cases and not used to construct this Figure. Vertical dashed line indicates the strain-at-break for polyamide layers like the ones in TFC membranes. Dotted trend lines are added as a guide for the reader.

4. Conclusions

Two commercial polyamide TFC membranes were used to estimate the effect of mechanical strain on their transport properties and ultimately their performance in PRO mode. Firstly, we showed that the global transport properties of the membranes did not change significantly after being subjected to linear strain typical of PRO operations. Secondly, using a newly developed burst pressure test for flat sheet membranes, we theorize that the increased salt passage through the membranes was attributable to local deformation in the membrane region along the border of the spacer opening. We defined a deformability coefficient to estimate the membrane strain at a known pressure in terms of easily attainable characteristics like opening size, membrane thickness and secant modulus (from stress-strain curve) and used it to postulate a solution diffusion model that accounts for defects by considering the deformability of the membrane in the experimental setup. The model was used to fit our PRO experimental data and numerous other data reported in the literature, which revealed that salt passage increases as membrane deformation increases. Along with this effect, there is a lowered mass-transfer resistance, which constitutes the tradeoff between mechanical deformation (associated with increased solute passage) and the mass-transfer resistance observed in pressurized OP. Our observations support the idea that the deformability coefficient and our solution diffusion model with defects can serve as guidelines for the design of membranes and modules for pressurized OP such as PRO, OARO, and PAFO. It may find use for niche applications such as patterning RO membranes or high-pressure RO used for ZLD.

Acknowledgements

The authors would like to thank DuPont Water and Process solutions for donating the SEAMAXX and SW30XLE membranes. We thank Mary Beth Fulton for early experiments on

measuring transport properties of deformed TFC membranes and Emily Vandale for assisting on measurements of burst pressure and deflection of TFC membranes. We acknowledge the use of the Clemson Electron Microscope Laboratory, Clemson Materials Physical Testing Lab, Clemson Light Imaging Facility, and Clemson Machining and Technical Services. This work was supported by funding from the National Science Foundation (NSF) under Award CBET-1510790. Opinions, findings, and conclusions or recommendations expressed in this material are those of the authors and do not necessarily reflect the views of the NSF.

Nomenclature

Letters

A	Membrane water permeance
A'	Membrane surface area
a_M	Spacer opening size
B	Membrane salt flux coefficient
c	Solution NaCl concentration
D	Diffusion coefficient of NaCl in Water
E_M	Membrane Young's Modulus
$E_{M,S}$	Membrane secant modulus
E_r	Membrane compressive reduced modulus
J	Flux
K	Deformability coefficient
K_A	Defect water permeance correction factor
k	Mass-transfer coefficient
l	Membrane Length
m	Mass
OA	Spacer relative open area
P	Pressure
R_M	Burst pressure cell opening radius
S	Membrane Structural Parameter
t	Time
t_m	Membrane thickness
V	Volume
w	Membrane deflection
w_0	Membrane maximum deflection
x	Position along spacer axis

Greek Letters

ε	Membrane strain
ν_M	Membrane Poisson's Ratio

π	Solution Osmotic Pressure
ρ	Density
σ	Stress
τ	Membrane Tortuosity
φ	Membrane Porosity
Subscripts	
A'	Surface area
l	Length
D	Draw solution
F	Feed solution
w	Water
s	Salt
$defect$	Flux through a defect
PRO	Measured in PRO test
RO	Measured in RO test
0	Initial (t=0)
h	At hold value
m	Maximum value
f	Final value
$local$	Calculated locally, i.e., at a defined x position

References

[1] T. V. Bartholomew, L. Mey, J.T. Arena, N.S. Siefert, M.S. Mauter, Osmotically assisted reverse osmosis for high salinity brine treatment, Desalination 421 (2017) 3–11. https://doi.org/10.1016/j.desal.2017.04.012.

[2] A. Achilli, A.E. Childress, Pressure retarded osmosis: From the vision of Sidney Loeb to the first prototype installation - Review, Desalination 261 (2010) 205–211. https://doi.org/10.1016/j.desal.2010.06.017.

[3] S. Sarp, J. Cho, Editorial of the special issue for pressure retarded osmosis, Desalination 389 (2016) 1. https://doi.org/10.1016/j.desal.2016.03.009.

[4] T.S. Chung, X. Li, R.C. Ong, Q. Ge, H. Wang, G. Han, Emerging forward osmosis (FO) technologies and challenges ahead for clean water and clean energy applications, Curr. Opin. Chem. Eng. 1 (2012) 246–257. https://doi.org/10.1016/j.coche.2012.07.004.

[5] S. Sahebi, S. Phuntsho, L. Tijing, G. Han, D.S. Han, A. Abdel-Wahab, H.K. Shon, Thin-film composite membrane on a compacted woven backing fabric for pressure assisted osmosis, Desalination 406 (2017) 98–108. https://doi.org/10.1016/j.desal.2016.06.001.

[6] J. Duan, E. Litwiller, I. Pinnau, Solution-diffusion with defects model for pressure-assisted forward osmosis, J. Membr. Sci. 470 (2014) 323–333. https://doi.org/10.1016/j.memsci.2014.07.018.

[7] T.Y. Cath, M. Elimelech, J.R. McCutcheon, R.L. McGinnis, A. Achilli, D. Anastasio, A.R. Brady, A.E. Childress, I. V. Farr, N.T. Hancock, J. Lampi, L.D. Nghiem, M. Xie, N.Y. Yip, Standard Methodology for Evaluating Membrane Performance in Osmotically Driven Membrane Processes, Desalination 312 (2013) 31–38.

https://doi.org/10.1016/j.desal.2012.07.005.
[8] D.L. Shaffer, J.R. Werber, H. Jaramillo, S. Lin, M. Elimelech, Forward osmosis: Where are we now?, Desalination 356 (2015) 271–284. https://doi.org/10.1016/j.desal.2014.10.031.
[9] G. Han, S. Zhang, X. Li, T.-S. Chung, Progress in pressure retarded osmosis (PRO) membranes for osmotic power generation, Prog. Polym. Sci. 51 (2015) 1–27. https://doi.org/10.1016/j.progpolymsci.2015.04.005.
[10] N.H.M. Ripin, P.S. Goh, W.J. Lau, A.F. Ismail, B.C. Ng, Pressure-Retarded Osmosis, in: Membr. Sep. Princ. Appl., Elsevier, 2019: pp. 339–359. https://doi.org/10.1016/B978-0-12-812815-2.00011-9.
[11] S. Sarp, Z. Li, J. Saththasivam, Pressure Retarded Osmosis (PRO): Past experiences, current developments, and future prospects, Desalination 389 (2016) 2–14. https://doi.org/10.1016/j.desal.2015.12.008.
[12] Y.C. Kim, J.H. Lee, S.J. Park, Novel crossflow membrane cell with asymmetric channels: Design and pressure-retarded osmosis performance test, J. Membr. Sci. 476 (2015) 76–86. https://doi.org/10.1016/j.memsci.2014.11.018.
[13] Y.C. Kim, M. Elimelech, Adverse impact of feed channel spacers on the performance of pressure retarded osmosis, Environ. Sci. Technol. 46 (2012) 4673–4681. https://doi.org/10.1021/es3002597.
[14] Q. She, D. Hou, J. Liu, K.H. Tan, C.Y. Tang, Effect of feed spacer induced membrane deformation on the performance of pressure retarded osmosis (PRO): Implications for PRO process operation, J. Membr. Sci. 445 (2013) 170–182. https://doi.org/10.1016/j.memsci.2013.05.061.
[15] K.L. Lee, R.W. Baker, H.K. Lonsdale, Membranes for power generation by pressure-retarded osmosis, J. Membr. Sci. 8 (1981) 141–171. https://doi.org/10.1016/S0376-7388(00)82088-8.
[16] A. Tiraferri, N.Y. Yip, A.P. Straub, S. Romero-Vargas Castrillon, M. Elimelech, A method for the simultaneous determination of transport and structural parameters of forward osmosis membranes, J. Membr. Sci. 444 (2013) 523–538. https://doi.org/10.1016/j.memsci.2013.05.023.
[17] N.N. Bui, J.T. Arena, J.R. McCutcheon, Proper accounting of mass transfer resistances in forward osmosis: Improving the accuracy of model predictions of structural parameter, J. Membr. Sci. 492 (2015) 289–302. https://doi.org/10.1016/j.memsci.2015.02.001.
[18] J.T. Arena, S.S. Manickam, K.K. Reimund, P. Brodskiy, J.R. McCutcheon, Characterization and Performance Relationships for a Commercial Thin Film Composite Membrane in Forward Osmosis Desalination and Pressure Retarded Osmosis, Ind. Eng. Chem. Res. 54 (2015) 11393–11403. https://doi.org/10.1021/acs.iecr.5b02309.
[19] T. Holt, E. Sivertsen, W.R. Thelin, G. Brekke, Pressure Dependency of the Membrane Structure Parameter and Implications in Pressure Retarded Osmosis (PRO), in: Osmotically Driven Membr. Process. - Approach, Dev. Curr. Status, InTech, 2018. https://doi.org/10.5772/intechopen.72444.
[20] J. Kim, B. Kim, D. Inhyuk Kim, S. Hong, Evaluation of apparent membrane performance parameters in pressure retarded osmosis processes under varying draw pressures and with draw solutions containing organics, J. Membr. Sci. 493 (2015) 636–644. https://doi.org/10.1016/j.memsci.2015.07.035.
[21] J. Lee, S. Kim, Predicting power density of pressure retarded osmosis (PRO) membranes

using a new characterization method based on a single PRO test, Desalination 389 (2016) 224–234. https://doi.org/10.1016/j.desal.2016.01.026.
[22] B. Kim, S. Lee, S. Hong, A novel analysis of reverse draw and feed solute fluxes in forward osmosis membrane process, Desalination 352 (2014) 128–135. https://doi.org/10.1016/j.desal.2014.08.012.
[23] K. Wang, A.A. Abdalla, M.A. Khaleel, N. Hilal, M.K. Khraisheh, Mechanical properties of water desalination and wastewater treatment membranes, Desalination 401 (2017) 190–205. https://doi.org/10.1016/j.desal.2016.06.032.
[24] J.Y. Chung, J.H. Lee, K.L. Beers, C.M. Stafford, Stiffness, strength, and ductility of nanoscale thin films and membranes: A combined wrinkling-cracking methodology, Nano Lett. 11 (2011) 3361–3365. https://doi.org/10.1021/nl201764b.
[25] ASTM International, ASTM Standard D882, 2018, Standard Test Method for Tensile Properties of Thin Plastic Sheeting, West Conshohocken, PA, 2018. https://doi.org/10.1520/D0882-18.
[26] J.A. Idarraga-Mora, M.A. Lemelin, S.T. Weinman, S.M. Husson, Effect of Short-Term Contact with C1–C4 Monohydric Alcohols on the Water Permeance of MPD-TMC Thin-Film Composite Reverse Osmosis Membranes, Membranes (Basel) 9 (2019) 92. https://doi.org/10.3390/membranes9080092.
[27] J.A. Idarraga-Mora, D.A. Ladner, S.M. Husson, Thin-film composite membranes on polyester woven mesh with variable opening size for pressure-retarded osmosis, J. Membr. Sci. 549 (2018) 251–259. https://doi.org/10.1016/j.memsci.2017.12.023.
[28] D.L. Shaffer, J.M. LaManna, D.L. Jacobson, D.S. Hussey, M. Elimelech, E.P. Chan, Studying water and solute transport through desalination membranes via neutron radiography, J. Membr. Sci. (2017) 0–1. https://doi.org/10.1016/j.memsci.2017.10.046.
[29] T.Y. Cath, M. Elimelech, J.R. McCutcheon, R.L. McGinnis, A. Achilli, D. Anastasio, A.R. Brady, A.E. Childress, I. V. Farr, N.T. Hancock, J. Lampi, L.D. Nghiem, M. Xie, N.Y. Yip, Standard Methodology for Evaluating Membrane Performance in Osmotically Driven Membrane Processes, Desalination 312 (2013) 31–38. https://doi.org/10.1016/j.desal.2012.07.005.
[30] B.S. Lalia, E. Guillen-Burrieza, H.A. Arafat, R. Hashaikeh, Fabrication and characterization of polyvinylidenefluoride-co-hexafluoropropylene (PVDF-HFP) electrospun membranes for direct contact membrane distillation, J. Membr. Sci. 428 (2013) 104–115. https://doi.org/10.1016/j.memsci.2012.10.061.
[31] W.K. Schomburg, Introduction to Microsystem Design, Springer Berlin Heidelberg, Berlin, Heidelberg, 2011. https://doi.org/10.1007/978-3-642-19489-4.
[32] J. Kováčik, Correlation between Poisson's ratio and porosity in porous materials, J. Mater. Sci. 41 (2006) 1247–1249. https://doi.org/10.1007/s10853-005-4237-0.
[33] M. Asmani, C. Kermel, A. Leriche, M. Ourak, Influence of porosity on Youngs modulus and poisson's ratio in alumina ceramics, J. Eur. Ceram. Soc. 21 (2001) 1081–1086. https://doi.org/10.1016/S0955-2219(00)00314-9.
[34] G. Han, T.S. Chung, M. Toriida, S. Tamai, Thin-film composite forward osmosis membranes with novel hydrophilic supports for desalination, J. Membr. Sci. 423–424 (2012) 543–555. https://doi.org/10.1016/j.memsci.2012.09.005.
[35] L. Brunet, D.Y. Lyon, K. Zodrow, J.C. Rouch, B. Caussat, P. Serp, J.C. Remigy, M.R. Wiesner, P.J.J. Alvarez, Properties of membranes containing semi-dispersed carbon nanotubes, Environ. Eng. Sci. 25 (2008) 565–575. https://doi.org/10.1089/ees.2007.0076.

[36] Y. Ma, F. Shi, W. Zhao, M. Wu, J. Zhang, J. Ma, C. Gao, Preparation and characterization of PSf/clay nanocomposite membranes with LiCl as a pore forming additive, Desalination 303 (2012) 39–47. https://doi.org/10.1016/j.desal.2012.07.016.
[37] A.P. Straub, N.Y. Yip, M. Elimelech, Raising the Bar: Increased Hydraulic Pressure Allows Unprecedented High Power Densities in Pressure-Retarded Osmosis, Environ. Sci. Technol. Lett. 1 (2013) 55–59. https://doi.org/10.1021/ez400117d.
[38] K.L. Hickenbottom, J. Vanneste, M. Elimelech, T.Y. Cath, Assessing the current state of commercially available membranes and spacers for energy production with pressure retarded osmosis, Desalination 389 (2016) 108–118. https://doi.org/10.1016/j.desal.2015.09.029.
[39] J.A. Idarraga-Mora, A.S. Childress, P.S. Friedel, D.A. Ladner, A. Rao, S. Husson, Role of Nanocomposite Support Stiffness on TFC Membrane Water Permeance, Membranes (Basel) 8 (2018) 111. https://doi.org/10.3390/membranes8040111.
[40] S.S. Manickam, J. Gelb, J.R. McCutcheon, Pore structure characterization of asymmetric membranes: Non-destructive characterization of porosity and tortuosity, J. Membr. Sci. 454 (2014) 549–554. https://doi.org/10.1016/j.memsci.2013.11.044.
[41] G.M. Geise, H.B. Park, A.C. Sagle, B.D. Freeman, J.E. McGrath, Water permeability and water/salt selectivity tradeoff in polymers for desalination, J. Membr. Sci. 369 (2011) 130–138. https://doi.org/10.1016/j.memsci.2010.11.054.
[42] N.Y. Yip, M. Elimelech, Performance limiting effects in power generation from salinity gradients by pressure retarded osmosis, Environ. Sci. Technol. 45 (2011) 10273–10282. https://doi.org/10.1021/es203197e.
[43] A.P. Straub, S. Lin, M. Elimelech, Module-scale analysis of pressure retarded osmosis: Performance limitations and implications for full-scale operation, Environ. Sci. Technol. 48 (2014) 12435–12444. https://doi.org/10.1021/es503790k.
[44] N.Y. Yip, M. Elimelech, Performance limiting effects in power generation from salinity gradients by pressure retarded osmosis, Environ. Sci. Technol. 45 (2011) 10273–10282. https://doi.org/10.1021/es203197e.
[45] M. Despotovic, V. Nedic, D. Despotovic, S. Cvetanovic, Evaluation of empirical models for predicting monthly mean horizontal diffuse solar radiation, Renew. Sustain. Energy Rev. 56 (2016) 246–260. https://doi.org/10.1016/j.rser.2015.11.058.
[46] Q. She, J. Wei, N. Ma, V. Sim, A.G. Fane, R. Wang, C.Y. Tang, Fabrication and characterization of fabric-reinforced pressure retarded osmosis membranes for osmotic power harvesting, J. Membr. Sci. 504 (2016) 75–88. https://doi.org/10.1016/j.memsci.2016.01.004.
[47] J. Wei, C. Qiu, C.Y. Tang, R. Wang, A.G. Fane, Synthesis and characterization of flat-sheet thin film composite forward osmosis membranes, J. Membr. Sci. 372 (2011) 292–302. https://doi.org/10.1016/j.memsci.2011.02.013.
[48] S.J. Kwon, S.H. Park, M.S. Park, J.S. Lee, J.H. Lee, Highly permeable and mechanically durable forward osmosis membranes prepared using polyethylene lithium ion battery separators, J. Membr. Sci. 544 (2017) 213–220. https://doi.org/10.1016/j.memsci.2017.09.022.
[49] Q. She, X. Jin, C.Y. Tang, Osmotic power production from salinity gradient resource by pressure retarded osmosis: Effects of operating conditions and reverse solute diffusion, J. Membr. Sci. 401–402 (2012) 262–273. https://doi.org/10.1016/j.memsci.2012.02.014.
[50] Y. Li, R. Wang, S. Qi, C.Y. Tang, Structural stability and mass transfer properties of

pressure retarded osmosis (PRO) membrane under high operating pressures, J. Membr. Sci. 488 (2015) 143–153. https://doi.org/10.1016/j.memsci.2015.04.030.
[51] Sterlitech Corporation, CF042 PERMEATE CARRIER, PTFE, 17 MIL, 5/PK, (n.d.). https://www.sterlitech.com/cf042-permeate-carrier-17mil.html (accessed August 10, 2019).
[52] X. Song, Z. Liu, D.D. Sun, Energy recovery from concentrated seawater brine by thin-film nanofiber composite pressure retarded osmosis membranes with high power density, Energy Environ. Sci. 6 (2013) 1199. https://doi.org/10.1039/c3ee23349a.
[53] N.N. Bui, J.R. McCutcheon, Hydrophilic nanofibers as new supports for thin film composite membranes for engineered osmosis, Environ. Sci. Technol. 47 (2013) 1761–1769. https://doi.org/10.1021/es304215g.
[54] N.N. Bui, J.R. McCutcheon, Nanofiber supported thin-film composite membrane for pressure-retarded osmosis, Environ. Sci. Technol. 48 (2014) 4129–4136. https://doi.org/10.1021/es4037012.
[55] ASTM International, ASTM Standard E11, 2017, Standard Specification for Woven Wire Test Sieve Cloth and Test Sieves, West Conshohocken, PA, 2017. https://doi.org/10.1520/E0011-17.
[56] J.R. McCutcheon, M. Elimelech, Influence of concentrative and dilutive internal concentration polarization on flux behavior in forward osmosis, J. Membr. Sci. 284 (2006) 237–247. https://doi.org/10.1016/j.memsci.2006.07.049.